



# Low effective fault strength due to frictional-viscous flow in phyllonites, Karakoram Fault Zone, NW India

David Wallis\*, Geoffrey E. Lloyd, Richard J. Phillips, Andrew J. Parsons, Richard D. Walshaw

School of Earth and Environment, University of Leeds, Leeds, LS2 9JT, UK

## ARTICLE INFO

### Article history:

Received 5 January 2015

Received in revised form

14 April 2015

Accepted 11 May 2015

Available online 20 May 2015

### Keywords:

Karakoram Fault Zone

Fault weakening

Frictional-viscous flow

Phyllonite

Deformation-fluid-metamorphism

interactions

Shear strength

## ABSTRACT

Phyllosilicate-rich fault rocks are common in large-scale fault zones and can dramatically impact fault rheology. Experimental evidence suggests that multi-mechanism frictional-viscous flow (FVF) may operate in such lithologies, potentially significantly weakening mature fault cores. We report microstructures indicative of FVF in exhumed phyllonites of the Karakoram Fault Zone (KFZ), NW India. These include interconnected muscovite foliae, lack of quartz/feldspar crystal preferred orientations, and sutured grains and overgrowths indicative of fluid-assisted diffusive mass transfer. FVF microphysical modelling, using microstructural observations from the natural fault rock and experimentally-derived friction and diffusion coefficients, predicts low peak shear strengths of <20 MPa within the frictional-viscous transition zone. Chlorite geothermometry indicates that synkinematic chlorites grew at  $351 \pm 34^\circ\text{C}$  (c. 10 km depth) during FVF, immediately above the transition to quartz crystal plasticity. The deformation processes and interpreted low shear strength of the exhumed KFZ fault rocks provide analogues for processes operating currently at depth in active faults of similar scale. If similar lithologies are present at depth, then the Quaternary seismic characteristics of the KFZ support faults with phyllonitic cores being able to accommodate large seismic ruptures. The results also provide rare rheological constraints for mechanical models of the India-Asia collision zone.

© 2015 The Authors. Published by Elsevier Ltd. This is an open access article under the CC BY license (<http://creativecommons.org/licenses/by/4.0/>).

## 1. Introduction

Constraints on fault rock rheology are fundamental to characterisation of deformation processes across a wide range of spatial and temporal scales, including micro-scale deformation mechanisms, earthquake nucleation/propagation, creeping behaviour, fault reactivation and macroscopic dynamics of continental crust/lithosphere (Rutter et al., 2001; Handy and Brun, 2004; Holdsworth, 2004; Bürgmann and Dresen, 2008; Imber et al., 2008; Schrank et al., 2008; Holdsworth et al., 2011). The presence of phyllosilicate-rich lithologies, including phyllonites and certain gouges and foliated cataclasites, in fault zones is thought to dramatically impact fault zone rheology (Wintsch et al., 1995; Jefferies et al., 2006a, 2006b; Holdsworth et al., 2011; Rutter et al., 2013; Wintsch et al., 2013). Phyllosilicates (e.g. micas and clays) and phyllosilicate-bearing fault rocks are

typically frictionally weak, with coefficients of friction ( $\mu$ ) commonly < 0.4 (Morrow et al., 2000; Moore and Lockner, 2004; Niemeijer and Spiers, 2005; Ikari et al., 2011; Behnken and Faulkner, 2012; den Hartog and Spiers, 2013; den Hartog et al., 2013). Such materials are typically associated with velocity strengthening behaviour, particularly at low sliding velocities (<1  $\mu\text{m s}^{-1}$ ), but velocity weakening behaviour can occur at higher sliding velocities (>1  $\mu\text{m s}^{-1}$ ) (Niemeijer and Spiers, 2005, 2006, 2007; Ikari et al., 2011; den Hartog and Spiers, 2013; den Hartog et al., 2013). Conversely, most other mineral groups, including framework silicates, and their associated fault rocks are frictionally strong with  $\mu = 0.6\text{--}0.85$  (Byerlee, 1978; Blanpied et al., 1995; Ikari et al., 2011). Fault materials with  $\mu > 0.5$  also exhibit both velocity strengthening and velocity weakening behaviour but, in general, are more prone to velocity weakening than those with lower frictional strength (Ikari et al., 2011).

In lithologies containing both phyllosilicates and stronger minerals, normal stress and strain-rate sensitive, multi-mechanism, frictional-viscous flow (FVF; Handy, 1990) has been proposed on the basis of experimental observations (Chester and Higgs, 1992; Bos et al., 2000; Bos and Spiers, 2001; Niemeijer and Spiers, 2005) and theoretical modelling (Chester, 1995; Bos

\* Corresponding author. Tel.: +441133432846.

E-mail addresses: [d.wallis@leeds.ac.uk](mailto:d.wallis@leeds.ac.uk) (D. Wallis), [eargel@leeds.ac.uk](mailto:eargel@leeds.ac.uk) (G.E. Lloyd), [r.j.phillips@leeds.ac.uk](mailto:r.j.phillips@leeds.ac.uk) (R.J. Phillips), [eeap@leeds.ac.uk](mailto:eeap@leeds.ac.uk) (A.J. Parsons), [r.d.walshaw@leeds.ac.uk](mailto:r.d.walshaw@leeds.ac.uk) (R.D. Walshaw).

and Spiers, 2002; Niemeijer and Spiers, 2007; den Hartog and Spiers, 2014). FVF occurs by frictional sliding on interconnected phyllosilicate foliae, which wrap around clasts of stronger minerals, whilst incompatibilities in the shear displacement field are accommodated by dilation and/or fluid-assisted diffusive mass transfer from high to low stress sites on clast grain boundaries (Fig. 1; Bos and Spiers, 2002). The effective strength of assemblages deforming by these combined mechanisms is subject therefore to control by phyllosilicate frictional strength and clast dissolution-precipitation kinetics, hence also normal stress, pore fluid pressure and chemistry, temperature, strain rate, composition, grain size and angles between sliding surfaces (Bos and Spiers, 2002; Niemeijer and Spiers, 2005).

FVF has the potential to result in dramatic weakening relative to Navier–Coulomb friction with Byerlee (1978) friction coefficients, or normal stress-independent plastic flow laws, particularly at the base of the upper crust in the frictional-viscous transition zone (FVTZ) where elevated temperatures enhance diffusional mass transfer (Chester, 1995; Bos and Spiers, 2002; Niemeijer and Spiers, 2005). Whilst FVF has a strong experimental and theoretical basis, an ongoing challenge is to model the rheology of frictional-viscous deformation of natural fault rocks. In order to assess the extent to which FVF weakens faults and the conditions under which this occurs in nature, detailed descriptions of fault rocks potentially deformed by FVF are required, in addition to constraints on the deformation conditions.

Microstructures consistent with the operation of FVF have been described from faults in compressional, extensional and strike-slip tectonic settings (summarised in Table 1). These studies show that FVF potentially operates most commonly in phyllonites and foliated cataclasites, but may occur also in schists, gouges and micaceous mylonitic lithologies. The conditions under which these fault rocks form and FVF may occur span a commensurately large range, typically 200–500 °C and 5–15 km depth, in broad agreement with the predictions of microphysical modelling (Bos and Spiers, 2002; Niemeijer and Spiers, 2005; den Hartog and Spiers, 2014). Many of the studies in Table 1 describe similar sequential fault rock evolution whereby fracturing results in grain size reduction and localized fluid influx. The ingressing fluids promote retrograde

hydration alteration of frictionally strong minerals (e.g. feldspars, pyroxenes) to weaker phyllosilicates (e.g. muscovite, chlorite, talc). The resultant phyllosilicates form interconnected weak layers that wrap around more rigid relict clasts, commonly showing pressure solution seams and overgrowths indicative of fluid assisted diffusive mass transfer (Table 1; see also Handy (1990) and White and Knipe (1978)).

Fault strength is an important factor for characterising the styles and mechanisms of continental deformation (Rutter et al., 2001; Handy and Brun, 2004; Bürgmann and Dresen, 2008). Whether, for instance, broad zones of continental deformation are best approximated by continuum deformation of thin viscous sheets, or as a collage of microplates/blocks, depends largely on the strength and significance of faults relative to the intervening crust (Tapponnier and Molnar, 1976; England and Houseman, 1988; Molnar, 1988; Thatcher, 2009). Faults with low shear strength relative to intervening material result in more localised deformation and kinematically complex strain fields during crustal/lithospheric-scale deformation. For the India-Asia collision zone, which is one of the principle testing grounds for such hypotheses, opinions range widely between these two end-members (Bürgmann and Dresen, 2008; Thatcher, 2009; Searle et al., 2011).

The Karakoram Fault Zone (KFZ) is one of the longest strike-slip faults of the Himalayan-Tibetan system and delineates the western margin of the Tibetan plateau (Fig. 2). As such, its history, mechanics and kinematics are central to discriminating between models of Tibetan deformation (Searle et al., 2011). Two schools of thought, based on geological evidence, exist for the long-term history of the KFZ. In one, the KFZ initiated as early as 19–32 Ma and has accommodated offsets of several hundred kilometres at slip-rates of  $\geq 10 \text{ mmyr}^{-1}$  (Lacassin et al., 2004; Valli et al., 2008; Boutonnet et al., 2012; Sen et al., 2014). In the other, the KFZ initiated at <16 Ma and has accumulated no more than 150 km offset at slip-rates of  $< 10 \text{ mmyr}^{-1}$  (Searle et al., 1998; Phillips et al., 2004; Wang et al., 2011; Zhang et al., 2011; Wallis et al., 2014a, 2014b). An alternative approach to investigating deformation of the India-Asia collision zone is to model its present-day deformation based on geodetic data and its current fault configurations (e.g. He and Chéry, 2008; Thatcher, 2009; Longstaff and Meade,

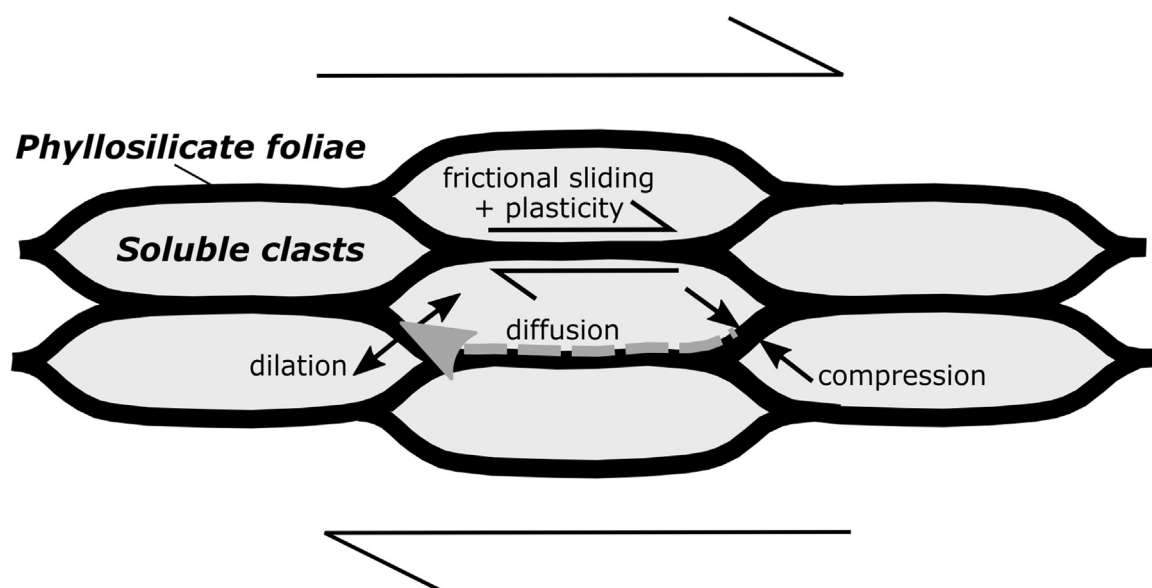


**Fig. 1.** Simplified sketch of frictional-viscous flow after Bos and Spiers (2002) and Niemeijer and Spiers (2005). Elongate soluble clasts (grey) are wrapped by phyllosilicate foliae (black). Clast material diffuses along grain boundaries from regions of compression to regions of dilation. Deformation within phyllosilicate foliae is accommodated by frictional sliding and/or intracrystalline plasticity.

**Table 1**

Summary of fault zones where frictional-viscous flow has been inferred or where reported microstructures suggest such deformation.

Fault	Fault rock	Frictional-viscous flow conditions	Source(s)
<i>Strike-slip Faults</i>			
Median Tectonic Line, Japan	Phyllonite Foliated cataclasite	c. 10 km depth c. 5 km depth 200–300 °C	Jefferies (2006b) Jefferies (2006a) Shigematsu et al. (2012)
Great Glen Fault, Scotland	Foliated cataclasite Phyllonite	8–15 km depth 250–450 °C	Stewart et al. (1999) Stewart et al. (2000) Holdsworth et al. (2001) Marsh et al. (2009)
Norumbega fault system, Maine	Act + Bt schist	400–500 °C	White (2001)
Siberia Fault Zone, New Zealand	Foliated cataclasite	8–10 km depth 200–250 °C	
Karakoram Fault Zone, India	Phyllonite	<14 km depth <400 °C	Wallis et al. (2013)
<i>Thrust Faults</i>			
Outer Hebrides Fault Zone, Scotland	Phyllonite	250–500 °C	Butler et al. (1995) Imber et al. (1997) Imber et al. (2001) Wibberley (2005) Wibberley (2005)
Ser Barbier Thrust, W. Alps	Phyllonite	Greenschist	
Moine Thrust Belt, Scotland	Foliated cataclasite & micaceous ultramylonite	5–9 km depth 250–350 °C	
<i>Extensional Faults</i>			
Err Detachment, Switzerland	Gouge	<300 °C	Manatschal (1999)
Zuccale Fault, Elba	Foliated cataclasite	<8 km depth <400 °C	Colletini and Holdsworth (2004) Colletini et al. (2009) Colletini et al. (2011)
Nordfjord-Sogn Detachment, Norway	Phyllonite	Greenschist	Braathen and Osmundsen (2004)
Wasatch Fault, Utah	Phyllonite	<350 °C	Parry et al. (1988)
Lake Char Fault, New England	Foliated cataclasite Phyllonite	<290 MPa Greenschist	Wintsch et al. (1995)

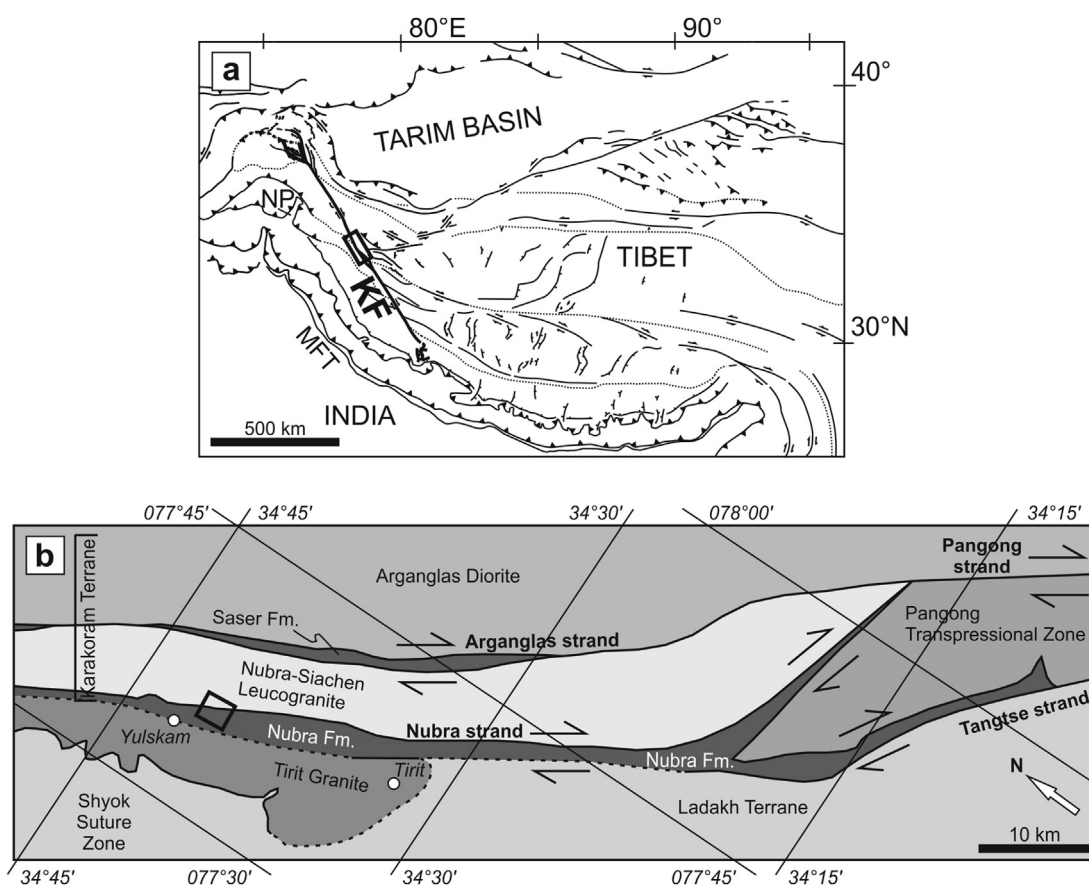


**Fig. 2.** a) Simplified sketch map of the major tectonic structures of the Himalaya-Tibet, showing the Karakoram Fault (KF, bold), Main Frontal Thrust (MFT), Nanga Parbat (NP), suture zones (dashed) and the location of b (bold box). b) Simplified sketch map of the geology of the Nubra Valley region of Ladakh, NW India. The bold box near Yulskam marks the location of Fig. 3. Modified from Phillips (2008).

2014). Such models predict fault slip-rates based on assumptions of either frictionless faults (e.g. Longstaff and Meade, 2014) or fault friction coefficients that are varied between model runs (e.g. He and Chéry, 2008). For instance, the modelling by He and Chéry (2008) predicts slip-rates for the KFZ that vary between c.  $1\text{--}13\text{ mm yr}^{-1}$  for friction coefficients of 0.60–0.02 respectively, approximately spanning the range of long-term slip-rates inferred from geological studies. Geological information on the shear strengths of major faults within the India-Asia collision zone is therefore required to constrain numerical model interpretations.

The style of deformation in the NW Himalaya has recently been suggested to be characterised by strain partitioning between arc-normal motion on the Main Frontal Thrust and arc parallel motion on the KFZ (Fig. 2), based on geological observations (Murphy et al., 2014) and GPS measurements (Kundu et al., 2014). GPS data indicate that, of the  $17 \pm 2\text{ mm yr}^{-1}$  convergence between India and Tibet,  $13.6 \pm 1\text{ mm yr}^{-1}$  is accommodated by the Himalayan thrust system whilst  $5 \pm 2\text{ mm yr}^{-1}$  is partitioned to dextral strike-slip motion on the KFZ (Kundu et al., 2014). This strain partitioning behaviour has been simulated by simple geodynamical models of the NW Himalaya region (Murphy et al., 2014; Whipp et al., 2014). Interestingly, the numerical models of Whipp et al. (2014) indicate that such strain partitioning only occurs when the strike-slip fault zone is very weak, with internal friction angles  $< 10^\circ$ , corresponding to friction coefficients  $< 0.18$ . Geological constraints on the shear strength of the KFZ are therefore required to test the validity of the strain partitioning models.

Wallis et al. (2013) described greenschist facies phyllonites within the KFZ and interpreted them to play a significant role in weakening this major strike-slip fault of the India-Asia collision zone. In this contribution we describe the microstructure of these phyllonites in detail and determine the temperature of their formation using geothermometry of synkinematic chlorites. Finally we model their effective shear strength during FVF using microstructural and environmental parameters from the natural fault zone in the experimentally-derived FVF model of Niemeijer and Spiers (2005). The results are discussed in terms of their implications for the strength and seismogenic processes of large-scale fault zones, as well as for modelling and characterising the macroscopic tectonics of continental deformation (e.g. the Himalayan-Tibetan orogen).

## 2. Structural setting of the Karakoram fault zone phyllonites

The KFZ is a c. 800 km long dextral strike-slip fault forming the western margin of the Tibetan Plateau (Fig. 2a). The presently exposed phyllonite that is the focus of this study was estimated by Wallis et al. (2013) to have formed at or since c. 14 Ma. However, as the KFZ likely cuts similar metapelitic lithologies at both higher (now eroded) and lower (still buried) structural levels, the deformation processes that it records are potentially analogous to those operating at depth, both earlier in its history and at the present day.

In Ladakh, NW India, the KFZ juxtaposes the eastern Karakoram terrane in the NE with the Ladakh arc terrane in the SW (Fig. 2b). The Karakoram terrane in this region consists of the predominantly amphibolite grade Eastern Karakoram Metamorphic Complex (EKMC), including the Nubra and Saser formations and Pangong Transpressional Zone, along with dioritic and leucogranitic intrusions of the Karakoram batholith (Fig. 2b, Streule et al., 2009; Phillips et al., 2013). These two intrusive suites were emplaced during an Early-Late Cretaceous phase of subduction-related magmatism and a mid-Miocene episode of crustal anatexis following the India-Asia collision (Phillips et al., 2013).

In the Nubra Valley, the Nubra Formation of the EKMC comprises an elongate  $50 \times 2.5\text{ km}$  band of metapelitic and

metavolcanic lithologies between the  $15.87 \pm 0.08\text{ Ma}$  Nubra-Siachen leucogranite (Karakoram terrane) to the NE and the Ladakh terrane to the SW (Fig. 2b) (Phillips et al., 2004). The Nubra Formation consists of greenschist facies metavolcanics and metapelitic lithologies of greenschist to mid-amphibolite grade, including slates, phyllites, kyanite-garnet-mica schist, andalusite-garnet-mica schist and local occurrences of marble and serpentinite pods (Fig. 3) (Wallis et al., 2013). Metavolcanics are found in the SW portion of the Nubra Formation and metapelites generally increase in metamorphic grade towards the NE. Foliation-parallel altered lamprophyre sheets with chilled margins intrude the Nubra Formation in Yulskam gorge (Fig. 3). Fossil fauna suggest that at least some of the Nubra Formation protoliths are Permian in age (Thakur et al., 1981).

The Nubra Formation records a range of deformational fabrics (mylonitic, phyllonitic and cataclastic) formed under varied conditions within the Nubra strand of the KFZ (Phillips and Searle, 2007; Wallis et al., 2013), all of which strike approximately parallel to the regional trend of the fault (c.  $140^\circ$ , Fig. 3). Mylonitic fabrics developed within metavolcanics and more intensely in the metapelites include quartz and feldspar dynamic recrystallisation microstructures indicative of deformation under upper-greenschist to lower-amphibolite grade conditions (Wallis et al., 2013). The mylonitic fabrics grade with increasing intensity towards the NE margin of the Nubra Formation where it contacts the Nubra-Siachen leucogranite, which is also strongly mylonitised (Phillips and Searle, 2007). The mylonitic fabrics are overprinted by both foliated cataclasites and a prominent 7–10 m wide band of orange-brown phyllonite close to the NE margin of the Nubra Formation (Figure 3, also Figure 4 of Wallis et al., 2013; Phillips and Searle, 2007), along with more minor phyllonitic bands distributed over several hundred metres from the leucogranite contact. The phyllonite has been recorded in Yulskam gorge (Fig. 3) and again in the Tirit gorge c. 15 km to the SE (Phillips and Searle, 2007; Wallis et al., 2013). In Yulskam gorge, the phyllonite is bounded by foliated cataclasites, however, cross-cutting relationships are difficult to determine in outcrop due to the sub-parallel lithological banding. The phyllonite consists of a greenschist facies assemblage of quartz, muscovite, albite, chlorite, rutile and minor Fe-oxides (Figs. 3 and 4), a lower grade assemblage than the amphibolite grade metapelites that it overprints. Wallis et al. (2013) suggested that phyllonitisation occurred at  $< 400^\circ\text{C}$  and noted that the phyllonite contains deformation microstructures potentially indicative of deformation by FVF. These include interconnected layers of muscovite and chlorite wrapped around clasts of albite and quartz that indent one another when in contact. The microstructures of the phyllonite are described in detail in the following section.

In Yulskam gorge, the kinematics of deformation in the Nubra Formation metavolcanics and metapelites are characterized by foliation with a mean orientation of  $142/76\text{ NE}$  and lineations with a mean orientation of  $17/137$  (Fig. 3). Dextral shear sense, indicated by S–C–C' fabrics, asymmetric mantled porphyroclasts and mica fish, is consistent with the dextral offset across the KFZ (Wallis et al., 2013). Shearing of the metapelites was therefore dominantly dextral strike-slip with a minor extensional component. The kinematics of deformation in the phyllonite band are characterized by foliation with a mean orientation of  $140/70\text{ SW}$  and lineations with a mean orientation of  $20/140$  (Fig. 3). The shear sense of the phyllonite is indicated by dextral S–C' fabrics (Wallis et al., 2013). The phase of deformation that affected the phyllonite was therefore dextral strike-slip with a subordinate reverse component.

Recrystallised quartz and calcite veins within the Nubra Formation, including the phyllonite (Fig. 4b), indicate episodic embrittlement events at depths where deformation was otherwise



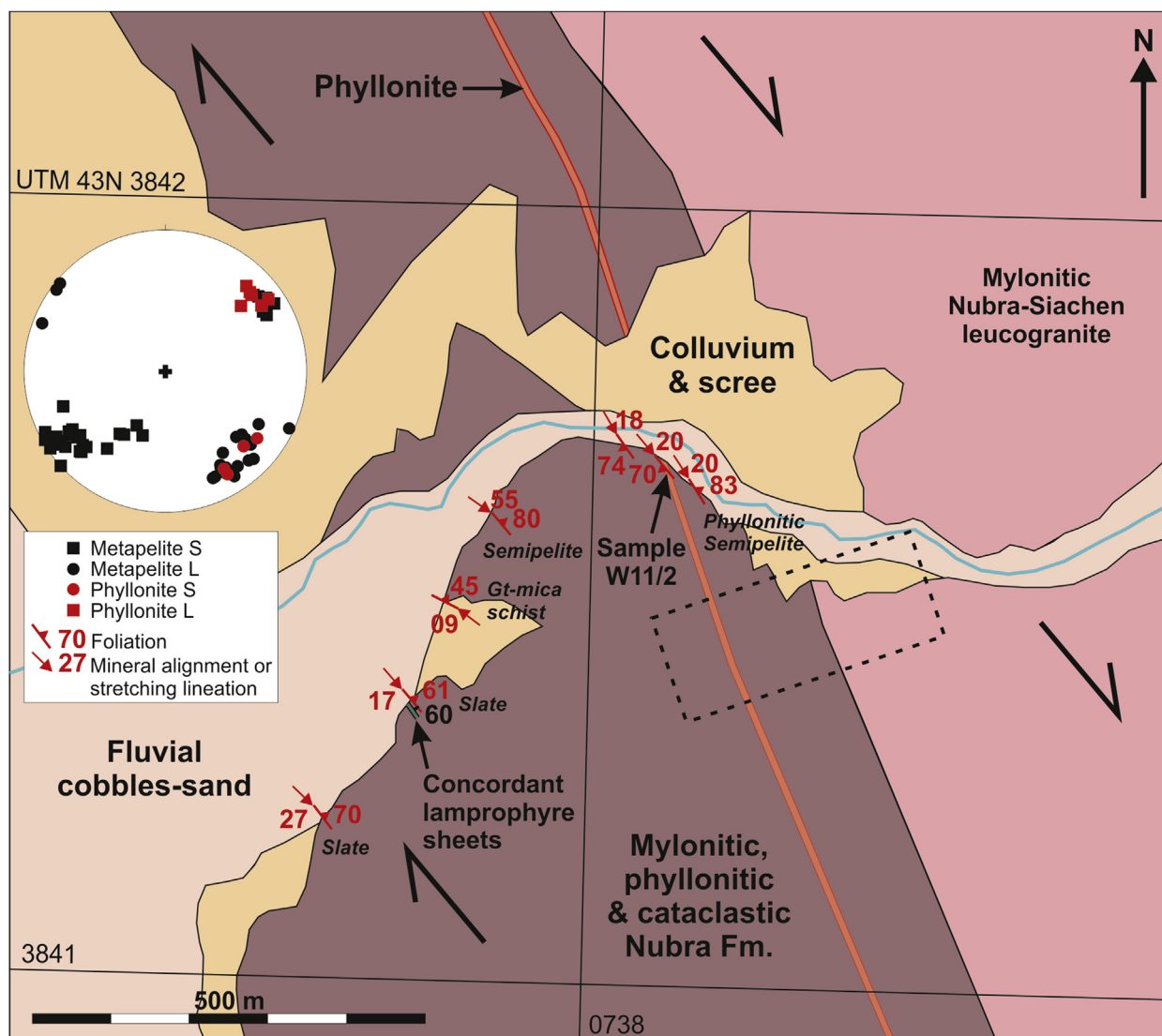


**Fig. 3.** Simplified geological map of the Nubra fault strand in Yulskam gorge, showing the studied band of phyllonite and sample location. Also shown are foliation (S) and lineation (L) measurements from the phyllonite and surrounding metapelites of the Nubra Formation. Figure 4a of Wallis et al. (2013) is marked by the dashed box.

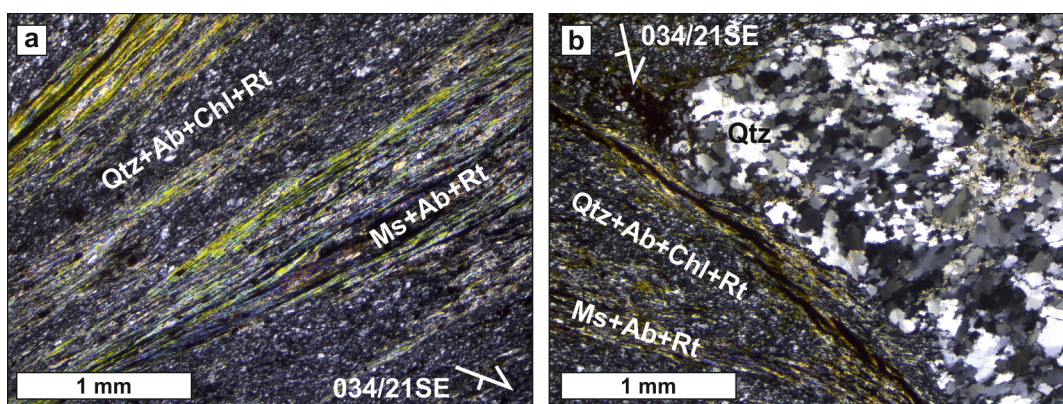


**Fig. 4.** Cross-polarised optical photomicrographs of the Nubra Formation phyllonite. a) Typical domainal phyllonitic structure consisting of quartz + albite + chlorite + rutile (Qtz + Ab + Chl + Rt) and muscovite + albite + rutile (Ms + Ab + Rt) bands. b) Quartz clast showing ubiquitous subgrains typical of subgrain rotation dynamic recrystallisation, within phyllonitic matrix.

predominantly ductile (Wallis et al., 2013). Such veining during mylonitic flow is diagnostic of low differential stress and high fluid pressures and therefore these brittle events were potentially aseismic (Handy et al., 2007). Minor brittle faults cross-cut the Nubra Formation at variable angles and record deformation at shallower depths after phyllonitisation (Wallis et al., 2013).

Palaeoseismic evidence for large ( $M_w > 6$ ) earthquakes in the vicinity of the Nubra strand of the KFZ includes Quaternary syndimentary lacustrine seismites and offset fluvio-lacustrine strata (Upadhyay, 2001, 2003; Phartiyal et al., 2005; Phartiyal and Sharma, 2009). Considerations based on wider Quaternary palaeoseismic evidence and the long-term slip-rate of the KFZ suggest that the central portion of the fault generates  $M_w$  7–8 earthquakes approximately every 1 kyr (Brown et al., 2002; Houlié and Phillips, 2013; Wallis et al., 2013). Evidence for Quaternary palaeoseismicity in the vicinity of the Nubra strand is noteworthy because at depth the KFZ likely cuts similar Karakoram Terrane lithologies to those presently exposed at the surface (e.g. Searle et al., 2010).

### 3. Phyllonite deformation microstructures and crystal fabrics

The KFZ phyllonite (sample W11/2, Fig. 3; Wallis et al., 2013) has a domainal microstructure (Figs. 4a and 5) of interlayered bands of quartz + albite + chlorite + rutile (Qtz + Ab + Chl + Rt, 60–70%) and muscovite + albite + chlorite + rutile (Ms + Ab + Chl + Rt, 30–40%). Quartz-rich domains consist of approximately 50% quartz, 30% albite and 20% randomly dispersed chlorite. Muscovite-rich bands are interconnected and laterally continuous at the thin section and hand specimen scales. Centimetre-scale folding of the layered microstructure (e.g. Figure 4c of Wallis et al., 2013) indicates that deformation was ductile at the hand specimen scale. In some instances individual bands consist of >95% aligned muscovite with asymmetric aligned rutile needles demonstrating dextral shear sense (Fig. 5b). More typically, the muscovite-rich bands consist of c. 70% aligned muscovite, which wraps around elongate clasts of albite (c. 20%) with interlayered rutile needles and chlorite sheets (Fig. 5c–d). The abundant rutile is likely derived from retrogression of biotite, which contains c. 2 wt.%  $\text{TiO}_2$  in preserved amphibolite-grade Nubra Formation metapelites (Wallis et al., 2014b). Chlorite is present as sheets intergrown with muscovite (Fig. 5c–d), but is best developed in the pressure shadows of albite clasts (Fig. 5e) and quartz-rich domains (Fig. 5f). These structures demonstrate that chlorite growth was syn-kinematic with respect to deformation of the phyllonite. The phyllonite also contains sigmoidal mm-scale clasts of dynamically recrystallised polycrystalline quartz (Fig. 4b). Ubiquitous subgrains and neoblasts of equal size within the quartz clasts indicate subgrain rotation dynamic recrystallisation. Elongate polyphase sigmoidal clasts composed of quartz + albite + chlorite + rutile are also present (Fig. 4a and f).

The results of two electron backscattered diffraction (EBSD) runs on the phyllonite sample are described in order to further characterise the phase distribution and to define the crystal fabrics within the specimen. EBSD data were collected using the FEI Quanta 650 FEG ESEM, equipped with an Oxford Instruments Nordlys S EBSD camera, Oxford Instruments Aztec 2.1 acquisition software and Channel 5 data processing software, at the University of Leeds. Pole figures were plotted using the program *Pfch5* (Mainprice, 1990). Data were collected using 20 kV accelerating voltage, 5–15 nA specimen current and 70° tilt angle. Two areas were analysed using automated beam scans. The first covers a region of both Qtz + Ab + Chl + Rt and Ms + Ab + Rt domains and was acquired with a 1075 × 940 grid of 0.763  $\mu\text{m}$  steps. The second provides a detailed analysis of a Ms + Ab + Rt domain and was acquired with a

468 × 409 grid of 0.895  $\mu\text{m}$  steps. Muscovite indexing rates were low compared to other phases due to the difficulty of preparing such muscovite-rich domains. Energy dispersive X-ray (EDX) maps acquired during EBSD analysis provide improved imaging of the elemental and hence phase distributions. Data were acquired on specimen surfaces cut parallel to the lineation and perpendicular to the foliation (i.e. the XZ plane of finite strain, with X horizontal in the images).

EBSD and EDX map analyses of the multi-domainal region shows interleaved Qtz + Ab + Chl + Rt and Ms + Ab + Rt domains a few hundred microns in thickness (Fig. 6a–f). The muscovite distribution is highlighted by the Al and K maps (Fig. 6c–d), whereas the albite distribution is highlighted by the Na map (Fig. 6e) and chlorite is highlighted in the Mg map (Fig. 6f). Pole figures of crystal orientations within a subset consisting of a Qtz + Ab + Chl + Rt domain, show that quartz and albite have very weak, close to random crystal orientations. Chlorite has a strong crystal preferred orientation (CPO) defined by <010> directions strongly aligned with X, {001} poles forming a YZ girdle with superposed maxima about Y and Z, and <100> directions forming maxima inclined c. 30° clockwise to X (Fig. 6g).

EBSD and EDX map analysis of the Ms + Ab + Rt domain shows scattered albite clasts distributed throughout a matrix of aligned muscovite (Fig. 6a–f). The muscovite distribution is highlighted by the Al and K maps (Fig. 6c–d), whereas the albite distribution is highlighted by the Na map (Fig. 6e) and chlorite is highlighted in the Mg map (Fig. 6f). Pole figure analysis (Fig. 6g) shows that muscovite has a strong CPO defined by {001} maxima parallel to Z, and <100> and <010> directions forming approximately XY girdles with superposed maxima parallel to X and Y. Albite has a weak and disordered CPO consisting of multiple scattered sub-maxima in each pole figure. Each sub-maximum likely corresponds to one, or a few, large clasts measured several times.

### 4. Interpretation of phyllonite deformation mechanisms

The shear strength of muscovite is known to be low over a wide range of conditions (Mariani et al., 2006; Niemeijer and Spiers, 2006, 2007; Van Diggelen et al., 2010; Behnsen and Faulkner, 2012; den Hartog and Spiers, 2013). The through-going nature of the muscovite-rich bands suggests therefore that deformation is likely to have been preferentially accommodated by these bands rather than the quartz-rich domains within the KFZ phyllonite. Within the most muscovite-rich (c. 95%) bands (Fig. 5b), deformation is interpreted to have been accommodated by frictional sliding on aligned muscovite cleavage planes, accompanied by dislocation glide on the (001)<110> slip system to produce the observed muscovite CPO. Within the muscovite + albite-rich bands (Fig. 5c–d), muscovite grain alignment and CPO suggests that sliding in the muscovite foliae was an important deformation mechanism (Fig. 6). Sutured/indented albite clasts (Fig. 5c–d, Fig. 6a) and chlorite fringes/overgrowths in pressure shadows (Fig. 5e–f) indicate that fluid-assisted diffusive mass transfer (i.e. pressure solution) was also significant in accommodating deformation. Poorly defined albite CPO (Fig. 6g) suggest that albite clasts deformed as relatively rigid bodies within the muscovite matrix. In combination, the sliding on muscovite foliae and diffusive processes indicated by sutured albite and chlorite overgrowths, along with the macroscopically ductile nature of deformation evidenced by folding, are strongly suggestive of frictional-viscous flow (Chester and Higgs, 1992; Chester, 1995; Bos et al., 2000; Bos and Spiers, 2001, 2002).

During frictional-viscous flow, sliding on aligned muscovite foliae accommodated the majority of strain. Albite clasts acted as passive rigid bodies, with volume incompatibilities removed by



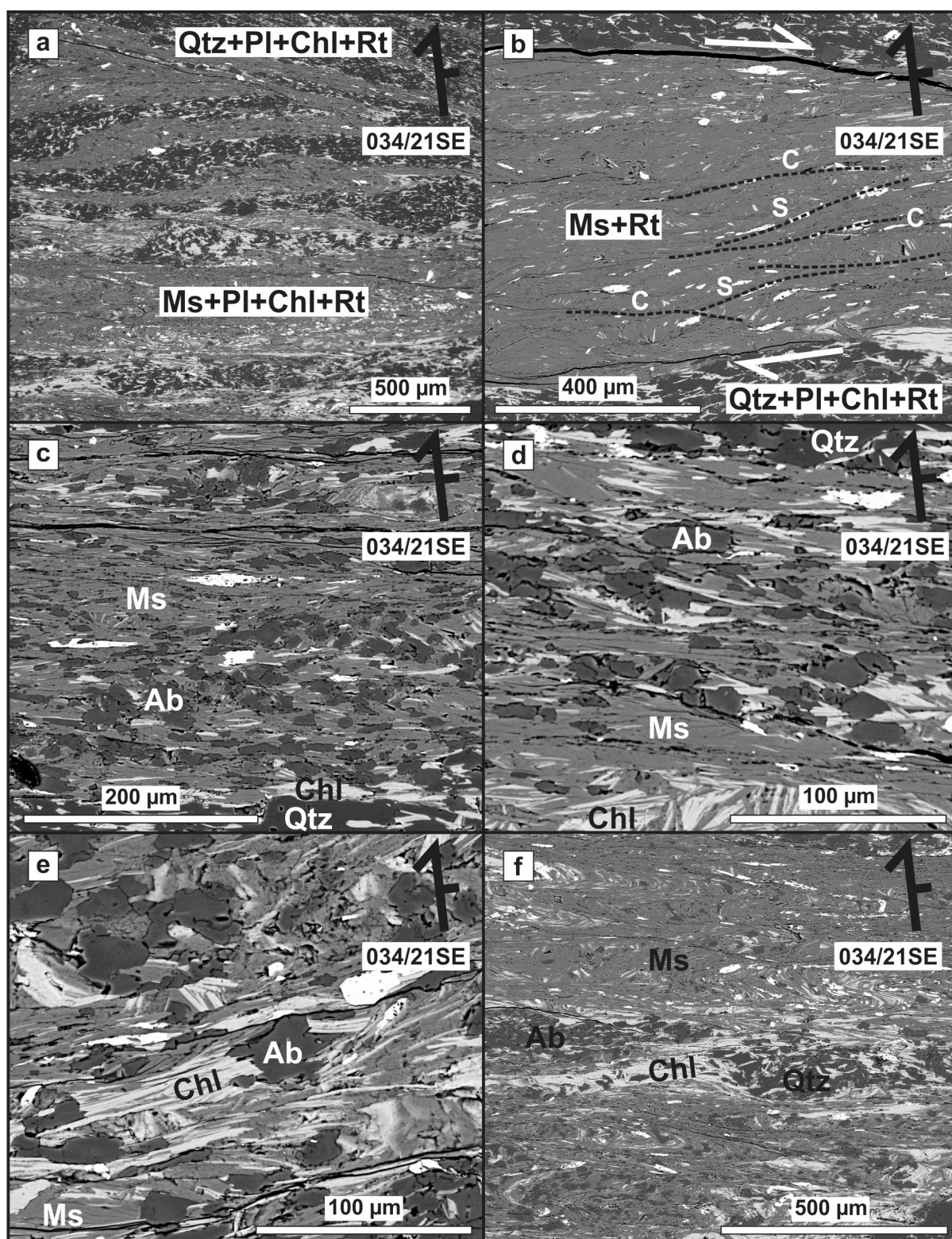


**Fig. 5.** Backscattered electron atomic number contrast images of the Karakoram Fault Zone phyllonite. a) Domainal microstructure of the phyllonite consisting of Ms + Ab + Chl + Rt and Qtz + Ab + Chl + Rt domains a few hundred microns thickness. b) Ms + Rt domain consisting of >95% Ms with aligned Rt needles (white) showing dextral asymmetry and S–C surfaces. c) Ms + Ab domains, showing slightly elongate albite clasts wrapped by aligned muscovite. d) Subordinate chlorite intergrowths are present in Ms + Ab domains. e) Chlorite fringes on albite clasts (centre) and sutured and indented albite grains (top left). f) Chlorite fringe on quartz-rich domain within Ms + Ab domain.

pressure solution when clasts become locked. Material was re-precipitated in low stress sites (including chloritic pressure shadows) at the dilational trailing edges of rigid albite clasts and quartz-rich domains. The differences in composition between

dissolved (e.g. albite) and precipitated (e.g. chlorite) phases suggest a component of incongruent pressure solution.

The chlorite CPO (Fig. 6) is consistent with a linear-decussate shape preferred orientation with (001) planes parallel to the X



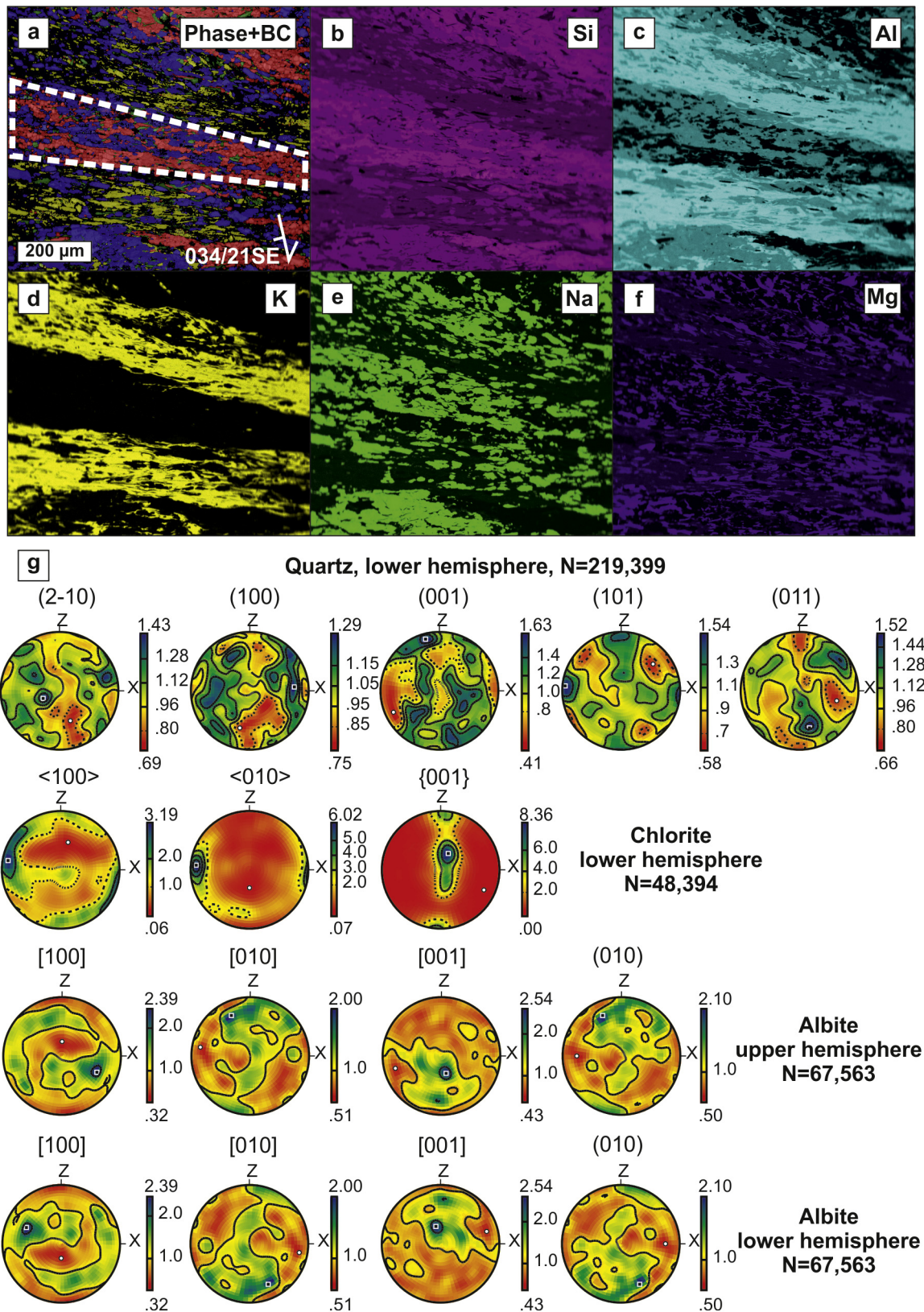


**Fig. 6.** Electron backscattered diffraction (EBSD) and energy dispersive X-ray (EDX) analysis of domainal phyllonite microstructure. a) EBSD diffraction pattern band contrast map overlain with phase map. Red-quartz, blue-albite, yellow-muscovite, green-chlorite, black-not indexed. Not indexed regions are primarily muscovite, as shown in the EDX maps. b-f) EDX element distribution maps of the same area as (a). Increased colour intensities qualitatively indicate increased elemental concentrations. b) Si distribution. c) Al distribution. d) K distribution highlights muscovite. e) Na distribution highlights albite. f) Mg distribution highlights chlorite. g) Pole figures of crystal orientations in map area in (a). Contours are in multiples of uniform distribution. (For interpretation of the references to colour in this figure legend, the reader is referred to the web version of this article.)



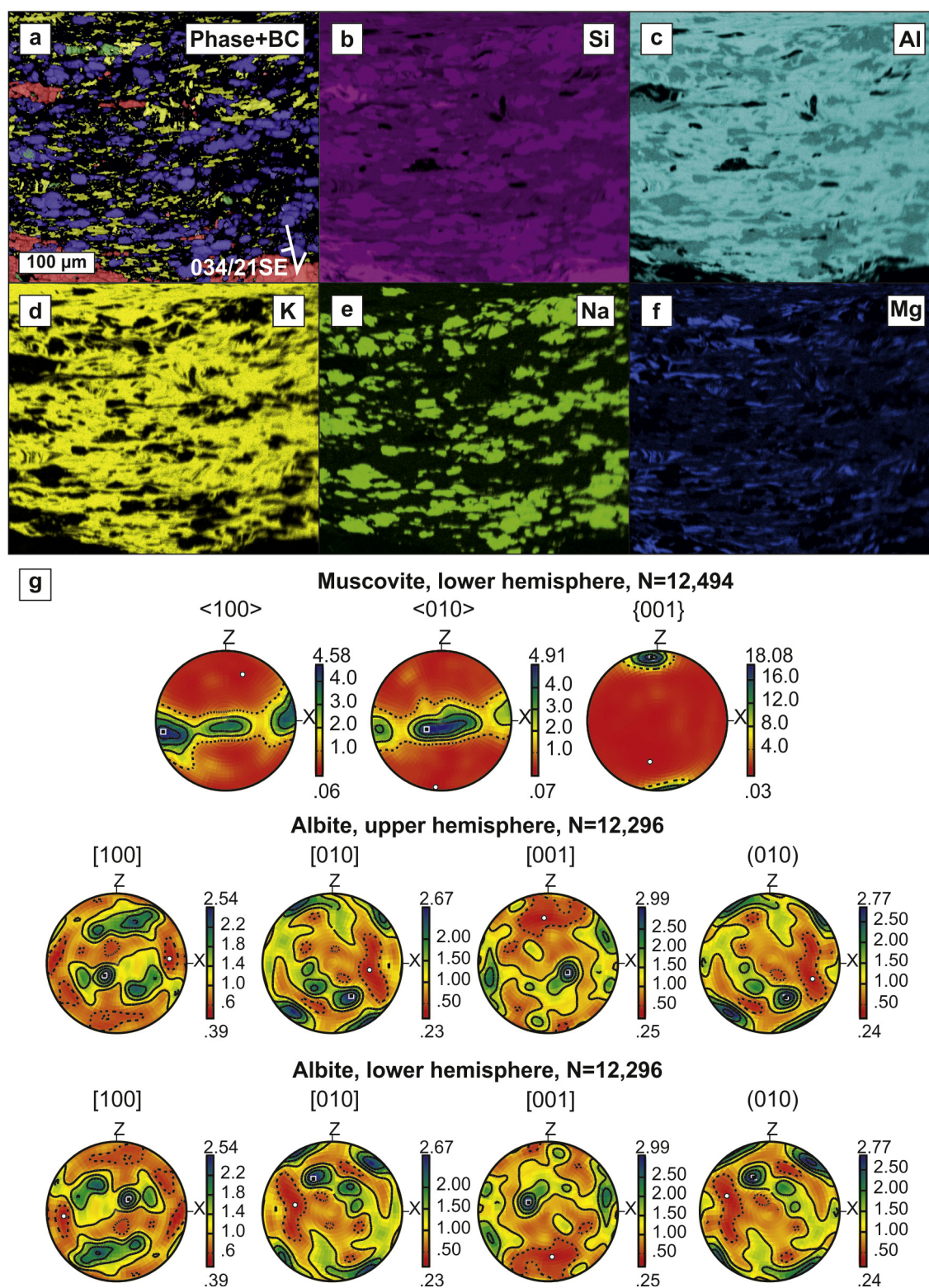


**Fig. 7.** Electron backscattered diffraction (EBSD) and energy dispersive X-ray (EDX) analysis of muscovite-rich domain. a) EBSD diffraction pattern band contrast map overlaid with phase map. Red-quartz, blue-albite, yellow-muscovite, green-chlorite, black-not indexed. Not indexed regions are primarily muscovite, as shown in the EDX maps. b-f) EDX element distribution maps of the same area as (a). Increased colour intensities qualitatively indicate increased elemental concentrations. b) Si distribution. c) Al distribution. d) K distribution highlights muscovite. e) Na distribution highlights albite. f) Mg distribution highlights chlorite. g) Pole figures of crystal orientations in quartz-rich domain marked in white in (a). Contours are in multiples of uniform distribution. (For interpretation of the references to colour in this figure legend, the reader is referred to the web version of this article.)

direction, as recognised in phyllonite from the Merens Fault in the Axial Zone of the Pyrenees (McCaig, 1987). The weak approximately XZ <100> and <010> girdles are consistent with this interpretation, whilst the superposed maxima parallel to X may suggest a component of dislocation glide (Fig. 6). It should be noted however that the data represent too few chlorite grains to draw any firm conclusions.

## 5. Chlorite chemistry and geothermometry

### 5.1. Chlorite compositions

Major element data were collected on chlorite using wavelength-dispersive X-ray spectroscopy on the Jeol 8230 electron microprobe at the University of Leeds. Chlorite analyses were collected using 15 kV accelerating voltage, 15 nA beam current and a 1  $\mu$  spot size. Peak and background count times were respectively 10 s and 5 s for Na and K, and 15 s and 7 s for remaining elements. Two to three analyses were made on each of 52 chlorite grains, giving 148 analyses in total (Supplementary Material).

Representative chlorite analyses are shown in Table 2. The chlorites are classified as ripidolite and pycnochlorite according to Hey (1954). Variation between analyses is small and suggests that the chlorites were well equilibrated (Neall and Phillips, 1987; Klein and Koppe, 2000). They have Fe/(Fe + Mg) in the range 0.56–0.61 and Si/Al in the range 0.90–1.05 (Table 2; Supplementary Material). Tetrahedral site occupation ranges between 5.08 and 5.93 Si and 2.07–2.92 Al<sup>IV</sup> per formula unit. The presence of abundant muscovite and albite suggests that the chlorites are saturated with respect to Al, whilst the presence of Fe-oxides suggests they are saturated also with respect to Fe.

### 5.2. Chlorite geothermometry

Chlorite geothermometry offers a means to estimate the temperature of chlorite growth within phyllonite. As chlorite growth is demonstrably synkinematic (Fig. 5e–f), chlorite geothermometry provides an estimate therefore of the deformation temperature.

**Table 2**  
Representative chlorite compositional analyses.

Analysis	C1	C2	C3	C4	C5	C6	C7	C8
<i>Oxide weight %</i>								
SiO <sub>2</sub>	23.80	23.64	23.36	23.02	23.98	23.80	23.50	21.81
TiO <sub>2</sub>	0.08	0.04	0.05	0.05	0.08	0.07	0.03	0.08
Al <sub>2</sub> O <sub>3</sub>	21.35	22.05	21.65	21.42	21.21	22.01	21.40	20.38
FeO*	28.21	28.26	28.48	28.43	28.72	28.56	28.10	28.00
MnO	0.39	0.44	0.41	0.42	0.41	0.38	0.34	0.00
MgO	11.16	10.96	11.46	11.31	11.36	11.28	11.02	11.54
CaO	0.01	0.07	0.03	0.03	0.08	0.01	0.02	0.01
Na <sub>2</sub> O	0.01	0.05	0.02	0.03	0.04	0.00	0.00	0.00
K <sub>2</sub> O	0.05	0.04	0.02	0.04	0.04	0.07	0.05	0.04
Total	85.06	85.55	85.48	84.75	85.92	86.18	84.46	81.86
<i>Cations per 28 oxygens</i>								
Si	5.29	5.22	5.17	5.15	5.29	5.22	5.26	5.08
Al <sup>IV</sup>	2.71	2.78	2.83	2.85	2.71	2.78	2.74	2.92
Al <sup>VI</sup>	2.87	2.96	2.82	2.81	2.80	2.91	2.90	2.67
Fe	5.24	5.22	5.28	5.32	5.30	5.24	5.26	5.45
Mn	0.07	0.08	0.08	0.08	0.08	0.07	0.07	0.00
Mg	3.69	3.61	3.79	3.78	3.73	3.69	3.68	4.00
Ca	0.00	0.02	0.01	0.01	0.02	0.00	0.00	0.00
Na	0.01	0.02	0.01	0.01	0.02	0.00	0.00	0.00
K	0.02	0.01	0.01	0.01	0.01	0.02	0.01	0.01
Ti	0.01	0.01	0.01	0.01	0.01	0.01	0.01	0.01
Total	19.91	19.93	20.01	20.03	19.97	19.94	19.93	20.14
Oct. total	11.87	11.87	11.97	11.99	11.91	11.91	11.91	12.12
Fe/(Fe + Mg)	0.59	0.59	0.58	0.59	0.59	0.59	0.59	0.58
Si/Al	0.95	0.91	0.92	0.91	0.96	0.92	0.93	0.91

Chlorite geothermometers are based on an empirical increase in Al<sup>IV</sup> content with increasing temperature (Cathelineau and Nieva, 1985; Cathelineau, 1988). Although there is a positive correlation between temperature and octahedral Fe, Fe and Mg contents are also strongly dependent on geological setting and solution composition (Cathelineau and Nieva, 1985; Cathelineau, 1988; Klein and Koppe, 2000). Kranidiotis and MacLean (1987) and Zang and Fyfe (1995) proposed modifications to the geothermometer of Cathelineau (1988) by adding corrections to the Al<sup>IV</sup> value as a function of the Fe/(Fe + Mg) ratio, for low (0.18–0.64) and high (0.78–0.81) values of the ratio respectively. This ratio would in turn be affected by the fluid to rock ratio, *f*O<sub>2</sub>, *f*S<sub>2</sub>, pH and hydrothermal fluid composition (Klein and Koppe, 2000).

Klein and Koppe (2000) summarised several criticisms of simple Al<sup>IV</sup>-based chlorite geothermometers, as follows. (1) Mixed layers and fine intergrowths can result in contamination of microprobe analyses by other minerals (Jiang et al., 1994). (2) Chlorites from different geological settings can show different temperature–composition relationships (De Caritat et al., 1993). (3) Chlorite and smectite represent a continuum between pure smectite (<180 °C) and chlorite (>270 °C) (Schiffman and Fridleifsson, 1991).

The chlorites in the KFZ phyllonite contain very low levels of Ca, Na and K (means < 0.2 atoms per formula unit) and cation totals on the octahedral site are very close to the ideal figure of 12 (11.87  $\pm$  0.16, 1 $\sigma$ ), suggesting that “contamination” by mixed layers or intergrowths is minimal in these analyses (Jiang et al., 1994; Klein and Koppe, 2000). Furthermore, the geological context of the phyllonites suggests that they formed at >270 °C (Wallis et al., 2013) and should therefore be close to pure chlorite (Schiffman and Fridleifsson, 1991). In order to address the variability of chlorite compositions between different geological settings we follow the procedure of Klein and Koppe (2000) in choosing the geothermometer for which the chlorite compositions of the calibration dataset most closely match those of the KFZ phyllonites (Table 3). The calibration of Cathelineau (1988) does not show a satisfactory match for the KFZ phyllonite chlorites as all of the key parameters are out of the calibration range (Table 3). Similarly, the geothermometer of Zang and Fyfe (1995) was calibrated using chlorites with higher Fe/(Fe + Mg) and Si/Al than those from the KFZ phyllonite (Table 3). Bourdelle et al. (2013) produced a geothermometric calibration incorporating the results of several recent studies and spanning a range of 1.70–2.42 Al<sup>IV</sup> per formula unit. The KFZ phyllonite chlorites however have considerably higher Al<sup>IV</sup> contents up to 2.92 per formula unit (Table 3).

The chlorites used to calibrate the geothermometer of Kranidiotis and MacLean (1987) are most similar to those of the KFZ phyllonite as they include compositions up to 2.83 Al<sup>IV</sup> per formula unit and the other parameters are highly comparable between the two datasets (Table 3). The Kranidiotis and MacLean (1987) geothermometer is therefore most appropriate for estimating the temperature of chlorite growth in the KFZ phyllonite. The error associated with this calibration, arising from the spread of measurements in the original Cathelineau and Nieva (1985) dataset, is estimated at  $\pm$  25 °C. The temperature estimate for chlorite growth in the KFZ phyllonite given by the Kranidiotis and MacLean (1987) calibration is 351  $\pm$  34 °C, with the reported error being the square root of the sum of the squares of the calibration error and two standard deviations of the individual temperature estimates ( $\pm$ 23 °C). Two important caveats to this temperature estimate are that the calculated temperature is slightly outside the calibration range, which extends up to c. 300 °C, and that the effect of pressure on chlorite Al<sup>IV</sup> is in general poorly constrained. The true uncertainty of the temperature estimate is likely therefore to be greater than that reported.



**Table 3**

Comparison between the compositions of chlorites (28 oxygen basis) from the Karakoram Fault Zone phyllonite and those in the calibration datasets of chlorite geothermometers. Compositions for [Bourdelle et al. \(2013\)](#) are those that the geothermometer was tested against as the compositions of the calibration dataset are not given. The temperatures estimated for the KFZ phyllonite chlorites are given with the quadratic error of the calibration error and two standard deviations of the results.

	KFZ phyllonite	Cathelineau (1988)	Kranidiotis and MacLean (1987)	Zang and Fyfe (1995)	Bourdelle et al. (2013)
Fe/(Fe + Mg)	0.56–0.61	0.24–0.37	0.18–0.64	0.78–0.81	0.08–0.88
Al <sup>IV</sup>	2.07–2.92	0.59–1.93	1.89–2.83	2.49–2.64	1.70–2.42
Si	5.08–5.93	2.80–3.41	5.17–5.80	5.36–5.51	
Si/Al	0.90–1.05	1.29–1.89	0.92–1.56	1.08–1.16	
T (°C)		308 ± 34	351 ± 34	284 ± 34	853 ± 2231

## 6. Frictional-viscous flow modelling

### 6.1. Microphysical modelling of frictional-viscous flow in the KFZ phyllonites

[Bos and Spiers \(2002\)](#) developed a microphysical model for FVF based on the results of kaolinite-halite analogue experiments ([Fig. 1](#); [Bos et al., 2000](#); [Bos and Spiers, 2001](#)). Halite was used in the experiments due to its well constrained diffusion kinetics at room temperature, allowing it to be used in room temperature experiments at reasonable rates as an analogue for pressure-dissolvable minerals under hydrothermal conditions. The model was then applied to quartz-muscovite assemblages. The model geometry and theoretical basis are described in detail by [Bos and Spiers \(2002\)](#), [Niemeijer and Spiers \(2005\)](#) and [Jefferies et al. \(2006a\)](#). [Niemeijer and Spiers \(2005\)](#) updated the original model, based on new experimental results from muscovite-halite mixtures, to incorporate the effects of a component of crystal plastic deformation within the phyllosilicate foliae. This revision is significant for the present study as the muscovite CPO ([Fig. 6](#)) suggests that at least a component of the deformation within the muscovite occurred by (001)<110> dislocation glide. Whilst these models are commonly invoked to describe deformation in mid-crustal phyllosilicate-rich lithologies (e.g. [Marsh et al., 2009](#); [Imber et al., 2008](#); [Colletini and Holdsworth, 2004](#)), their application to specific natural fault rocks has been limited to date. [Jefferies et al. \(2006a, 2006b\)](#) applied the model of [Bos and Spiers \(2002\)](#) to phyllonites and foliated cataclasites of the Median Tectonic Line, Japan, in which there was no evidence for phyllosilicate crystal plasticity. The [Niemeijer and Spiers \(2005\)](#) model on the other hand offers a means to estimate the approximate effective shear strength ( $\tau$ ) of the KFZ phyllonites, incorporating the effects of phyllosilicate crystal plasticity, during FVF in the upper-to mid-crust.

The model describes the effective shear strength ( $\tau$ ) of an assemblage undergoing FVF by the equation

$$\tau = \left\{ (\tau_{gb})^{-20} + (\tau_{pl})^{-20} \right\}^{-0.05} + \left\{ (\tau_{ps})^{-20} + (\tau_{dil})^{-20} \right\}^{-0.05} \quad (1)$$

where  $\tau_{gb}$  is the shear resistance due to frictional slip along phyllosilicate grain boundaries,  $\tau_{pl}$  is the shear resistance due to crystal plasticity in the phyllosilicate foliae,  $\tau_{ps}$  is the shear resistance resulting from pressure solution of the rigid clasts and  $\tau_{dil}$  is the shear resistance resulting from dilation of the model microstructure. The exponents of  $-20$  and  $-0.05$  (i.e.  $-1/20$ ) allow the model to accurately reproduce the experimentally observed transitions between regimes dominated by each of these deformation processes, whilst allowing the strength behaviour of the system to be represented using a single continuous function

([Niemeijer and Spiers, 2005](#)). Each of these components are defined respectively as:

$$\tau_{gb} = P\mu_{gb}\sigma_n \quad (2)$$

$$\tau_{pl} = \frac{1}{\alpha} \log \left\{ \frac{3^{0.5}\dot{\gamma}_{pl}}{C_{exp}(-Q/RT)} \right\} \quad (3)$$

$$\tau_{ps} = \frac{RTd}{B^2k_{s,p}\Omega_s} \dot{\gamma} \quad (4)$$

$$\tau_{dil} = 0.5(\sigma_1 - \sigma_3) \sin \left( \tan^{-1} \left( 1/\mu_{gb} \right) \right) \quad (5)$$

where  $P$  is the proportion of clast grain boundary area undergoing sliding,  $\mu_{gb}$  is the phyllosilicate grain boundary friction coefficient,  $\sigma_n$  (Pa) is the effective normal stress,  $C$  ( $s^{-1}$ ) and  $\alpha$  ( $Pa^{-1}$ ) are empirical constants taken from [Kronenberg et al. \(1990\)](#),  $\dot{\gamma}_{pl}$  ( $s^{-1}$ ) is the shear strain rate in phyllosilicate foliae,  $\dot{\gamma}$  ( $s^{-1}$ ) is the bulk assemblage shear strain rate,  $Q$  ( $Jmol^{-1}$ ) is the apparent activation energy,  $R$  ( $Pam^{-3} K^{-1} mol^{-1}$ ) is the molar constant,  $T$  (K) is the absolute temperature,  $d$  (m) is the average diffusion distance (grain size),  $B$  is the aspect ratio of clasts,  $k_{s,p}$  ( $mol m^{-3} s^{-1}$ ) is the rate coefficient for dissolution (s) or precipitation (p),  $\Omega_s$  ( $m^3 mol^{-1}$ ) is the molar volume of solid and  $\sigma_1 - \sigma_3$  (Pa) is the differential stress.

Equation (1) describes the shear strength as the combination of resistance from grain boundary friction, phyllosilicate dislocation glide, clast pressure-solution and microstructural dilation. Values for the parameters in Equations (2)–(5) are taken as defined by [Niemeijer and Spiers \(2005\)](#) for strike-slip faults, except where they can be modified for the composition and environmental conditions of the KFZ phyllonite, as defined in [Table 4](#).  $P = 0.6$  was visually estimated from the approximate proportion of foliation parallel grain boundaries in EBSD and EDX maps ([Fig. 6](#)) and backscattered electron images ([Fig. 5](#)). Values of  $d = 4.3 \mu m$  ( $n = 3510$ ) and  $B = 1.6$  were determined using the automated grain size statistics of the Channel 5 software for albite in the EBSD map area of [Fig. 6a](#). The molar volume of albite ( $1.0006 \times 10^{-4} m^3 mol^{-1}$ ) was taken from the database of [Holland and Powell \(1998\)](#). Temperatures were calculated according to a geothermal gradient of  $35^\circ C km^{-1}$ , corresponding to that estimated by [Wallis et al. \(2014b\)](#) from geothermobarometry of c. 17 Ma migmatites within the EKMC. Where possible, and within reasonable limits of uncertainty, values are chosen that will produce a maximum effective shear strength such that the modelled strength profile approximates an upper strength limit. For instance, the chosen value for  $\mu_{gb}$  is 0.38 (see below), determined by [Behnsen and Faulkner \(2012\)](#) for a muscovite aggregate in the presence of pore fluids and confining pressure. This value is broadly consistent with values of  $\mu = 0.3$ – $0.4$  for muscovite aggregates sheared at temperatures up to  $700^\circ C$  ([Mariani et al., 2006](#)). However, the coefficient of friction for

**Table 4**  
Values used in equations (1)–(5) for frictional-viscous flow modelling of the Karakoram Fault Zone phyllonite and the strike-slip model of Niemeijer and Spiers (2005).

Variable		Niemeijer and Spiers (2005) strike-slip model	KFZ phyllonite model	Source of values for KFZ phyllonite model
$P$	Proportion of grain boundary undergoing sliding	0.75	0.6	Estimated proportion of foliation parallel grain boundaries from EBSD maps and backscattered electron images, also appropriate for grains with aspect ratio of 1.6
$\mu_{gb}$	Grain boundary friction coefficient	0.31	0.38	Friction coefficient of wet muscovite aggregate from Behnen and Faulkner (2012) taken as an upper limit of possible values for muscovite in the KFZ phyllonite
$T$	Absolute temperature, from geothermal gradient	$25^\circ\text{C km}^{-1}$	$35^\circ\text{C km}^{-1}$	Miocene geothermal gradient estimated from geothermobarometry of Wallis et al. (2014b)
$d$	Average diffusion distance	$10\text{ }\mu\text{m}$	$4.3\text{ }\mu\text{m}$	EBSD map grain statistics: mean albite grain size
$B$	Aspect ratio of clasts	4.0	1.6	EBSD map grain statistics: mean aspect ratio of albite
$\Omega_s$	Molar volume of solid	$2.2668 \times 10^{-5}\text{ m}^3\text{ mol}^{-1}$	$1.0006 \times 10^{-4}\text{ m}^3\text{ mol}^{-1}$	Molar volume of albite from Holland and Powell (1998)
$\sigma_n$	Effective normal stress	0–345 MPa	0–345 MPa	Niemeijer and Spiers (2005)
$C$	Empirical constant	$4.6 \times 10^{-6}\text{ s}^{-1}$	$4.6 \times 10^{-6}\text{ s}^{-1}$	Niemeijer and Spiers (2005); Kronenburg et al. (1990)
$\alpha$	Empirical constant	$0.41\text{ MPa}^{-1}$	$0.41\text{ MPa}^{-1}$	Niemeijer and Spiers (2005); Kronenburg et al. (1990)
$\dot{\gamma}$	Bulk assemblage shear strain rate	$10^{-10}$ – $10^{-12}\text{ s}^{-1}$	$10^{-10}$ – $10^{-12}\text{ s}^{-1}$	Niemeijer and Spiers (2005), appropriate for KFZ phyllonite with 1–10 m thickness and 1–10 mm/yr slip rate
$Q$	Apparent activation energy	$5.1 \times 10^4\text{ kJ mol}^{-1}$	$5.1 \times 10^4\text{ kJ mol}^{-1}$	Niemeijer and Spiers (2005); Kronenburg et al. (1990)
$R$	Molar gas constant	$8.314\text{ JK}^{-1}\text{ mol}^{-1}$	$8.314\text{ JK}^{-1}\text{ mol}^{-1}$	Niemeijer and Spiers (2005)
$K_{s,p}$	Rate coefficient for dissolution/precipitation	$2.5 \times 10^{10}$ – $8.1 \times 10^{18}\text{ mol m}^{-3}\text{ s}^{-1}$	$2.5 \times 10^{10}$ – $8.1 \times 10^{18}\text{ mol m}^{-3}\text{ s}^{-1}$	Niemeijer and Spiers (2005)
$(\sigma_1 - \sigma_3)$	Differential stress	0–414 MPa	0–414 MPa	Niemeijer and Spiers (2005)

individual muscovite (001) surfaces is likely considerably lower than those of granular aggregates (Bos and Spiers, 2002).  $K_{s,p}$  values for quartz were used in the absence of such data for albite.

Effective shear strengths (Fig. 8) were calculated for Coulomb friction ( $\mu = 0.6$  and  $0.1$ ), and FVF of the albite-muscovite assemblage between 0 and 20 km depth following Niemeijer and Spiers (2005). Hydrostatic pore fluid pressures are assumed throughout. However, evidence for supra-hydrostatic fluid pressures within the Nubra strand of the KFZ suggests that the modelled effective normal stress distribution is an upper limit such that the results again provide a maximum effective shear strength. The strength of quartz undergoing dislocation creep was also calculated using the wet quartzite flow law of Luan and Paterson (1992) rewritten for simple shear by Bos and Spiers (2002).

## 6.2. Effective shear strength of the KFZ phyllonites

The modelling of the KFZ phyllonite predicts its effective shear strength during strike-slip deformation between 0 and 20 km depth (Fig. 8), assuming that the mineral assemblage and strain rate were to remain constant across all depths. Mineral transformations and changes in strain rate that are expected to occur at depths other than those at which the phyllonite formed mean however that the model results are most appropriate for the  $351 \pm 34^\circ\text{C}$  temperature range and should be treated with caution outside this range. For instance, although FVF is always weaker than quartz dislocation creep at equivalent strain rate, the phyllonite protoliths at greater depth may lack the necessary phyllosilicate content for FVF, such that quartz dislocation creep is an important deformation mechanism at  $> 11\text{ km}$  depth. Uncertainty in the model results is difficult to quantify due to the large number of variables, some of which have poorly constrained values/uncertainties themselves. The least well constrained parameters are the diffusion- and crystal plasticity-related variables, as discussed by Bos and Spiers (2002).

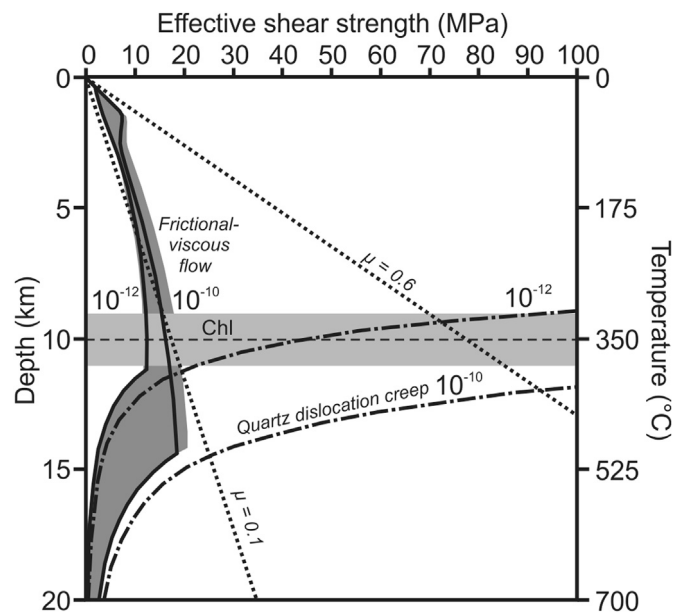


**Fig. 8.** FVF strength–depth plot for the Nubra Formation phyllonite (bold curves), calculated for strain rates of  $10^{-10}\text{ s}^{-1}$  and  $10^{-12}\text{ s}^{-1}$  according to equations (1)–(5), and Niemeijer and Spiers (2005). The dark grey envelope summarises the range of values discussed in the text arising from different strain rate–friction coefficient combinations. Also shown are the shear strength lines for Coulomb friction coefficients ( $\mu$ ) of 0.6 and 0.1 (dotted), and quartz undergoing viscous dislocation creep at strain rates of  $10^{-10}\text{ s}^{-1}$  and  $10^{-12}\text{ s}^{-1}$  (dot-dashed), following Bos and Spiers (2002) and Luan and Paterson (1992). Hydrostatic pore fluid pressures are assumed throughout. Temperature scale and modelling assumes a Miocene geothermal gradient of  $35^\circ\text{C km}^{-1}$  (Wallis et al., 2014b). Horizontal dashed line and light grey shaded region show the  $351 \pm 34^\circ\text{C}$  temperature range determined by chlorite geothermometry.



and Niemeijer and Spiers (2005). Changes in the strain rate estimate affect the FVF effective shear strength most at  $< 3$  km and  $> 11$  km depth, where shear strength is dominantly controlled by pressure solution and dislocation glide respectively, with greater shear resistance at higher strain rates. Within the  $351 \pm 34$  °C range of chlorite temperatures, shear strength is controlled primarily by the frictional strength of muscovite, reduced by crystal plasticity. In this temperature range shear strength is not greatly affected by changes in strain rate due to the frictional control.

Niemeijer and Spiers (2005) defined four deformation regimes, A–D, in which shear strength is dominated by (A) plasticity of phyllosilicate foliae, (B) frictional sliding in/on phyllosilicate foliae, (C) clast pressure-solution and (D) dilation-accommodated sliding respectively (Fig. 9). The elevated Miocene geothermal gradient within the Karakoram terrane (c.  $35$  °Ckm $^{-1}$ ; Wallis et al., 2014b) facilitates fluid-assisted diffusive mass transfer and dislocation glide such that the KFZ phyllonite FVF strength is lower than in the generalised case calculated by Niemeijer and Spiers (2005, Figure 9) and that estimated for phyllonite from the Median Tectonic Line, Japan, by Jefferies et al. (2006a), both of which assumed a geothermal gradient of  $25$  °Ckm $^{-1}$ . Enhanced phyllosilicate plasticity results in significantly reduced flow strength in regime A, and more modest strength reduction in regime B where deformation is instead dominated by frictional sliding on the phyllosilicate foliae. The depth extent and shear strength of Regime C is significantly reduced in the KFZ phyllonite model relative to that of Niemeijer and Spiers (2005) due to enhanced pressure solution. Whilst pressure-solution of the albite clasts was an important microstructural process, it added little additional shear resistance, such that the FVF strength of the albite-muscovite assemblage is not

significantly different from that of pure muscovite at depths of  $< 5$  km (Fig. 8). This emphasises the need for further experimental constraints on both the rheology of muscovite over the wide range of crustal conditions and, also, the dissolution/precipitation kinetics of albite. The latter should constrain the extent to which dissolution, diffusion or precipitation rates differ from those of quartz and which step is rate-limiting for pressure-solution under mid-crustal conditions.

The chlorite geothermometry results constrain the active FVF in the KFZ phyllonite to  $351 \pm 34$  °C (i.e. c. 9–11 km depth, Fig. 8). The primary control on the FVF strength of the assemblage, and its uncertainty, under these conditions is the muscovite friction coefficient. Behnken and Faulkner (2012) summarized experimentally determined friction coefficients for muscovite aggregates, which range between 0.35 and 0.47 in the presence of pore fluids. This range results in effective shear strengths of 15.5–18.6 MPa at  $10^{-10}$  s $^{-1}$  and 12.0–13.8 MPa at  $10^{-12}$  s $^{-1}$  at 10 km depth. Following the results of Behnken and Faulkner (2012) we take a friction coefficient of 0.38 as being typical (Table 4), which gives maximum shear strengths of 16.3 and 12.5 MPa at the same depth and strain rates respectively (Fig. 8). However, as discussed by Bos and Spiers (2002), friction on single muscovite cleavage planes, as in the model geometry, may be as low as 0.12 or even less, depending upon normal stress and environmental conditions. Nonetheless, the relatively high proportion of muscovite in the bands in which it occurs suggests that aggregate, rather than single crystal, friction coefficients may be more appropriate for this lithology.

These modelling results constrain the effective shear strength of only a volumetrically small portion of the fault zone (i.e. limited extent in both depth and thickness). Nonetheless, the depth range at which the phyllonite formed is commonly inferred to be the strongest portion of crustal fault zones (Sibson, 1986; Scholz, 1988; Holdsworth, 2004; Imber et al., 2008) and, in which case, is the portion that dominates total crustal fault zone shear strength and where the effects of weakening may be most pronounced. The rheology of the phyllonite, whilst at its depth of formation and FVF, is likely therefore to have significantly influenced the macroscopic behaviour of the fault zone.

## 7. Discussion

### 7.1. Deformation-metamorphism-fluid interactions and implications for fault zone rheology

Retrograde phyllonitisation of the Nubra Formation within the KFZ provides an example of interactions and feedbacks between deformation, metamorphism and fluid processes within a large-scale strike-slip fault zone. Peak kyanite-grade metamorphism ( $622 \pm 41$  °C) and regional deformation of the Nubra Formation occurred prior to the  $15.87 \pm 0.08$  Ma intrusion of the Nubra-Siachen leucogranite and associated andalusite-grade contact metamorphism at c. 500 °C and c. 320–330 MPa (Phillips et al., 2004; Reichardt and Weinberg, 2012; Wallis et al., 2014b). Mylonitic deformation within the Nubra strand of the KFZ had largely ceased to affect the Nubra-Siachen leucogranite by  $13.73 \pm 0.34$  Ma (Phillips et al., 2004). Deformation of the adjacent Nubra Formation continued however after this time, as it records mylonitic deformation to lower temperatures (c. 400 °C) than those affecting the leucogranite (c. 500 °C; Phillips and Searle, 2007; Wallis et al., 2013).

Continued syn-kinematic exhumation and cooling of the Nubra Formation resulted in greenschist facies phyllonitisation at  $351 \pm 34$  °C, characterised by the breakdown of biotite and synkinematic growth of muscovite and chlorite. The localised (7–10 m wide) nature of the principle phyllonite band suggests that this

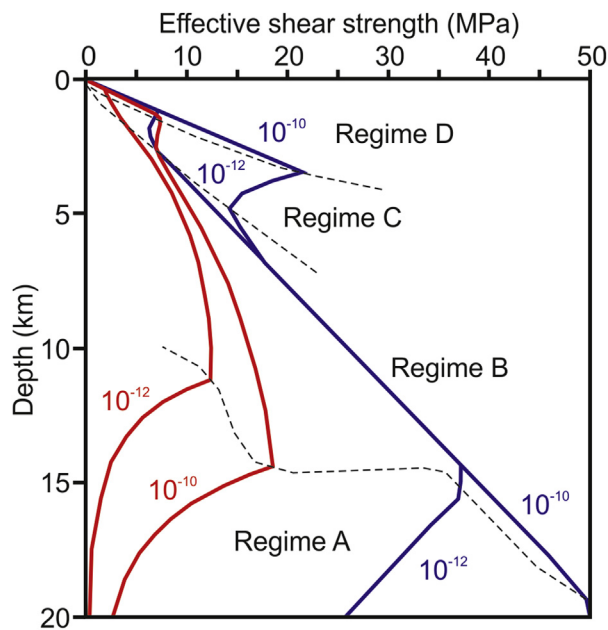


**Fig. 9.** Comparison between modelled strength of the KFZ phyllonite with a  $35$  °Ckm $^{-1}$  geothermal gradient (red) and the modelling of Niemeijer and Spiers (2005) for a quartz-muscovite assemblage within a transcurrent fault with a  $25$  °Ckm $^{-1}$  geothermal gradient (blue). Strain rates of  $10^{-10}$  s $^{-1}$  and  $10^{-12}$  s $^{-1}$  are shown for both cases. Also shown are deformation regimes A–D of Niemeijer and Spiers (2005), in which the modelled strength is dominated by (A) phyllosilicate plasticity, (B) frictional sliding in/on phyllosilicate foliae, (C) pressure-solution and (D) dilation-accommodated sliding respectively (boundaries shown as dashed black lines). Blue lines converge in regime B due to negligible impact of strain rate-sensitive mechanisms within regime where strength is controlled by frictional-sliding. (For interpretation of the references to colour in this figure legend, the reader is referred to the web version of this article.)

was a zone of locally elevated fluid flux (Wallis et al., 2013), presumably resulting from increased permeability induced by preceding deformation, as suggested by sheared quartz veins preserved within the non-phyllonitised metapelitic mylonites. The abundant muscovite within the phyllonite, along with the action of grain boundary fluids, allowed FVF to occur with lower shear resistance than quartz crystal plasticity at the same temperature (Fig. 8), causing quartz and albite to behave as relatively rigid clasts. The low effective shear strength (<20 MPa) of the phyllonite undergoing FVF, further enhanced strain localisation to within the phyllonite band.

Dynamic recrystallisation microstructures preserved in relict quartz clasts (Fig. 4b) demonstrate that the phyllonite was derived from an originally mylonitic protolith. Several previous studies of phyllonite (e.g. Great Glen Fault, Scotland, Stewart et al., 2000; Median Tectonic Line, Japan, Jefferies et al., 2006a; Shigematsu et al., 2012; Zuccale Fault, Elba, Collettini and Holdsworth, 2004) have documented evidence for cataclasis that triggered fluid influx, resulting in the growth of low friction phyllosilicates and the onset of fluid-assisted diffusive mass transfer processes. Brittle deformation did affect the Nubra Formation mylonites prior to phyllonitisation, as recrystallised quartz and calcite veins provide evidence for episodic embrittlement events, likely driven by elevated pore fluid pressures (Wallis et al., 2013). This is supported by the recrystallised quartz vein clast within the phyllonite. The lack of CPOs in quartz and albite, even within the more competent quartz-rich domains (Fig. 6g), also suggest that the rock may have undergone cataclasis following mylonitisation but prior to phyllonitisation. The lack of CPOs in the quartz-rich domains may also result however from a range of other deformation processes (e.g. grain boundary sliding) during pre-phyllonitisation deformation. From these (micro)structures, the following generalised sequence of events during exhumation and cooling can be inferred:

- Mylonitic deformation of the Nubra Formation metapelites (c. 400–550 °C),
- Localised transient fracturing events and fluid penetration due to elevated pore fluid pressure,
- Vein precipitation resulting from fluid-assisted diffusive mass transfer and pore fluid pressure drops during fracturing,
- Continued mylonitic deformation and dynamic recrystallisation of vein material (c. 400–500 °C),
- Retrograde reaction and phyllosilicate formation, with shear leading to phyllonitisation ( $351 \pm 34$  °C), potentially along a pre-existing fracture network such as that associated with vein formation.
- Frictional-viscous flow within the phyllonite ( $351 \pm 34$  °C).

Experimental observations of FVF show that it is associated with velocity strengthening behaviour characteristic of aseismic creep (Bos et al., 2000; Bos and Spiers, 2001, 2002; Niemeijer and Spiers, 2007; den Hartog et al., 2013; den Hartog and Spiers, 2013, 2014). This is consistent with cm-scale folds in the KFZ phyllonite that demonstrate that its deformation was dominantly ductile at the hand-specimen scale. However, Imber et al. (2008) argue that localized, potentially seismic, frictional slip may be common within phyllonitic fault cores due to factors such as elevated pore fluid pressure, stress/strain rate fluctuations around geometric irregularities and/or reorganization of the phyllosilicate network during changes in boundary conditions and slip vector. Analogue experiments have demonstrated that assemblages undergoing FVF can display marked velocity weakening and develop cataclastic microstructures when subjected to high sliding velocities ( $>1 \mu\text{m s}^{-1}$ , Niemeijer and Spiers, 2006, 2007). Such findings suggest that creeping phyllonite fault cores may be able to accommodate

propagating seismic ruptures that nucleate within internal domains of velocity weakening material (such as the quartz-rich domains of the KFZ phyllonite) or in adjacent lithologies (such as the Nubra-Siachen leucogranite within the Nubra strand). Niemeijer and Vissers (2014) reached similar conclusions based on geological and seismological observations and experimental data from phyllosilicate-rich gouges representing deformation at shallower depths of c. 4 km. For earthquakes to occur, such velocity weakening domains must be large enough for nucleating ruptures to reach a critical length, which depends upon effective normal stress and frictional properties of the material (Scholz, 2002). Such critical nucleation lengths are c. 1–10 m for deformation at a few kilometres depth (Niemeijer and Vissers, 2014), suggesting that nucleation within the mm-scale quartz-rich domains of the KFZ phyllonite is unlikely to have occurred at depths where FVF operated. Nonetheless, the surrounding leucogranite and metasediments are more than large enough to have hosted seismic rupture nucleation.

Whilst evidence for localised and potentially seismogenic frictional slip (e.g. through-going principle slip surfaces) is lacking within the KFZ phyllonites, cataclasis-filled faults are abundant within the adjacent leucogranite and cross-cut the Nubra Formation as later structures formed at shallower depths (Phillips and Searle, 2007; Wallis et al., 2013). Similarly, palaeoseismic evidence suggests that large magnitude ( $M_w > 6$ ) Quaternary earthquakes have occurred in the vicinity of the Nubra strand (Upadhyay, 2001, 2003; Phartiyal et al., 2005; Phartiyal and Sharma, 2009), which is likely to contain similar active fault rocks (including phyllonites) at depth to those exposed at the surface and continues to deform with dominantly dextral strike-slip kinematics, similar to the exhumed phyllonites (Phillips and Searle, 2007). It is probable therefore that localized brittle slip did affect the phyllonites intermittently, but that evidence for it has been obscured by subsequent FVF. Such considerations suggest that whilst the principle deformation mechanism of the phyllonite was FVF, the phyllonite band may have been able to accommodate seismic ruptures.

## 7.2. Constraining fault strength in models of Himalayan-Tibetan tectonics

Fault friction is an important consideration for mechanical models for deformation of the Tibetan Plateau. The 3D mechanical modelling of He and Chéry (2008) predicts KFZ slip-rates of between c. 1–13 mm/yr when friction coefficients are varied between 0.60 and 0.02. The results of the present study suggest that the FVF shear strength of the central KFZ at c. 10 km depth is comparable to that produced by a Coulomb friction coefficient of 0.1 (Fig. 8). He and Chéry (2008) also suggest that a friction coefficient of 0.1 provides the best general fit between their model predictions and geological constraints on the slip-rates of the Karakoram, Altyn Tagh and Kunlun faults. For this friction coefficient, the He and Chéry (2008) models predict KFZ slip-rates of c. 7–10 mm/yr. These rates are broadly equivalent to the slower long-term slip-rates of c. 4–10 mm/yr for the central KFZ derived from geological observations (Searle et al., 1998; Phillips et al., 2004) and compiled Quaternary slip-rates of  $> 5$ –11 mm/yr from the southern KFZ (Chevalier et al., 2012). However, it should be noted that there are considerable ranges of both faster and slower long-term, Quaternary and present day slip-rate estimates for the KFZ (see compilation by Searle et al., 2011). It is not the purpose of this discussion to discriminate between these slip rates but rather to highlight the need for further geological constraints on the strength of major faults to inform mechanical models of large-scale tectonic processes. Concomitantly, improved experimental constraints on the fundamental mechanics and chemical kinetics of deformation



processes are required to reduce the uncertainties associated with microphysical modelling.

FVF within the KFZ phyllonite appears to operate at sufficiently low shear stresses (approximating a Coulomb friction coefficient of 0.1) to be consistent with models of strain partitioning in the NW Himalaya, which require friction coefficients < 0.18 in the KFZ (Whipp et al., 2014). Such strain partitioning has been suggested to translate the NW Himalaya towards the western Himalayan syntaxis, contributing to rapid uplift and exhumation of the Nanga Parbat massif (Whipp et al., 2014). This study suggests that FVF within phyllonite provides a plausible weakening mechanism to facilitate these large-scale geodynamical processes. The growing geological evidence for FVF controlling the shear strength of the mid-crustal portions of major faults further suggests that incorporation of FVF-type rheologies into large-scale mechanical models is an important contemporary research objective.

## 8. Conclusions

Phyllonites in the Nubra strand of the Karakoram Fault Zone record evidence for deformation-fluid-metamorphism interactions that resulted in low effective shear strength within the frictional-viscous transition zone. Transient fluid-related fracture events in exhuming mylonitic metapelites promoted greenschist facies phyllonitisation and development of through-going muscovite-rich domains. Frictional-viscous flow within these domains occurred at  $351 \pm 34$  °C with modelled effective shear strengths of <20 MPa. The phyllonites are inferred to have deformed predominantly by aseismic creep. Potential for velocity weakening behaviour at high sliding velocities however suggests that earthquake ruptures may have been able to propagate within the phyllonite. The presence of the phyllonite band does not therefore preclude large magnitude earthquakes within the fault zone with subsequent healing and re-phyllonitisation of the microstructure. The low effective shear strength of the KFZ phyllonite is broadly consistent with mechanical models of the macroscopic tectonics of the Tibetan Plateau and NW Himalaya. Further geological investigations into the shear strengths of major faults in the India-Asia collision zone are required to ground-truth such models and characterise the long-term deformation of the region.

## Acknowledgements

Chlorite compositional data and geothermometry results are available as [Supplementary Material](#). Data used to construct Figs. 7 and 8 are available on request from the corresponding author. DW acknowledges support from NERC (training grant NE/I528750/1). Thanks to Bob Holdsworth and André Niemeijer for their detailed and constructive reviews. We thank Mark Handy and Chris Spiers for their comments on previous versions of the manuscript.

## Appendix A. Supplementary data

Supplementary data related to this article can be found at <http://dx.doi.org/10.1016/j.jsg.2015.05.010>.

## References

- Behnen, J., Faulkner, D.R., 2012. The effect of mineralogy and effective normal stress on frictional strength of sheet silicates. *J. Struct. Geology* 42, 49–61.
- Blanpied, M.L., Lockner, D.A., Byerlee, J.D., 1995. Frictional slip of granite at hydrothermal conditions. *J. Geophys. Res.-Solid Earth* 100, 13045–13064.
- Bos, B., Peach, C.J., Spiers, C.J., 2000. Frictional-viscous flow of simulated fault gouge caused by the combined effects of phyllosilicates and pressure solution. *Tectonophysics* 327, 173–194.
- Bos, B., Spiers, C.J., 2001. Experimental investigation into the microstructural and mechanical evolution of phyllosilicate-bearing fault rock under conditions favouring pressure solution. *J. Struct. Geology* 23, 1187–1202.
- Bos, B., Spiers, C.J., 2002. Frictional-viscous flow of phyllosilicate-bearing fault rock: microphysical models and implications for crustal strength profiles. *J. Geophys. Res. Solid Earth* 107, 2028.
- Bourdelle, F., Parra, T., Chopin, C., Beyssac, O., 2013. A new chlorite geothermometer for diagenetic to low-grade metamorphic conditions. *Contrib. Mineral. Petrol.* 165, 723–735.
- Bouttonnet, E., Leloup, P.H., Arnaud, N., Paquette, J.-L., Davis, W.J., Hattori, K., 2012. Synkinematic magmatism, heterogeneous deformation, and progressive strain localization in a strike-slip shear zone: the case of the right-lateral Karakorum fault. *Tectonics* 31, TC4012.
- Braathén, A., Osmundsen, P.T., 2004. Dynamic development of fault rocks in a crustal-scale detachment: an example from western Norway. *Tectonics* 23, TC4010.
- Brown, E.T., Bendick, R., Bourlès, D.L., Gaur, V., Molnar, P., Raisbeck, G.M., Yiou, F., 2002. Slip rates of the Karakorum fault, Ladakh, India, determined using cosmic ray exposure dating of debris flows and moraines. *J. Geophys. Res. Solid Earth* 107 (B9), 2192.
- Bürgmann, R., Dresen, G., 2008. Rheology of the lower crust and upper mantle: evidence from rock mechanics, geodesy, and field observations. *Annu. Rev. Earth Planet. Sci.* 36, 531–567.
- Butler, C.A., Holdsworth, R.E., Strachan, R.A., 1995. Evidence for Caledonian sinistral strike-slip motion and associated fault zone weakening, Outer Hebrides Fault Zone, NW Scotland. *J. Geol. Soc.* 152, 743–746.
- Byerlee, J., 1978. Friction of rocks. *Pure Appl. Geophys.* 116, 615–626.
- Cathelineau, M., 1988. Cation site occupancy in chlorites and illites as a function of temperature. *Clay Miner.* 23, 471–485.
- Cathelineau, M., Nieva, D., 1985. A chlorite solid solution geothermometer: the Los Azufres (Mexico) geothermal system. *Contrib. Mineral. Petrol.* 91, 235–244.
- Chester, F.M., 1995. A rheologic model for wet crust applied to strike-slip faults. *J. Geophys. Res. Solid Earth* 100, 13033–13044.
- Chester, F.M., Higgs, N.G., 1992. Multimechanism friction constitutive model for ultrafine quartz gouge at hypocentral conditions. *J. Geophys. Res. Solid Earth* 97, 1859–1870.
- Chevalier, M.L., Tapponnier, P., Van der Woerd, J., Ryerson, F.J., Finkel, R.C., Li, H.B., 2012. Spatially constant slip rate along the southern segment of the Karakorum fault since 200 ka. *Tectonophysics* 530, 152–179.
- Collettini, C., Holdsworth, R.E., 2004. Fault zone weakening and character of slip along low-angle normal faults: insights from the Zuccale fault, Elba, Italy. *J. Geol. Soc. Lond.* 161, 1039–1051.
- Collettini, C., Viti, C., Smith, S.A.F., Holdsworth, R.E., 2009. Development of interconnected talc networks and weakening of continental low-angle normal faults. *Geology* 37, 567–570.
- Collettini, C., Niemeijer, A., Viti, C., Smith, S.A.F., Marone, C., 2011. Fault structure, frictional properties and mixed-mode fault slip behavior. *Earth Planet. Sci. Lett.* 311, 316–327.
- De Caritat, P., Hutcheon, I., Walshe, J.L., 1993. Chlorite Geothermometry: a review. *Clays Clay Minerals* 41, 219–239.
- den Hartog, S.A.M., Niemeijer, A.R., Spiers, C.J., 2013. Friction on subduction megathrust faults: beyond the illite-muscovite transition. *Earth Planet. Sci. Lett.* 373, 8–19.
- den Hartog, S.A.M., Spiers, C.J., 2013. Influence of subduction zone conditions and gouge composition on frictional slip stability of megathrust faults. *Tectonophysics* 600, 75–90.
- den Hartog, S.A.M., Spiers, C.J., 2014. A microphysical model for fault gouge friction applied to subduction megathrusts. *J. Geophys. Res. Solid Earth* 119, 1510–1529.
- England, P.C., Houseman, G.A., 1988. The mechanics of the Tibetan Plateau. *Philos. Trans. R. Soc. Lond. A* 326, 301–319.
- Handy, M.R., 1990. The solid-state flow of polymineralic rocks. *J. Geophys. Res. Solid Earth Planets* 95, 8647–8661.
- Handy, M.R., Brun, J.P., 2004. Seismicity, structure and strength of the continental lithosphere. *Earth Planet. Sci. Lett.* 223, 427–441.
- Handy, M.R., Hirth, G., Bürgmann, R., 2007. Fault structure and rheology from the frictional-viscous transition downward. In: Handy, M.R., Hirth, G., Hovius, N. (Eds.), *Tectonic Faults – Agents of Change on a Dynamic Earth*, Dahlem Workshop Report, 95. The MIT Press, Cambridge, USA, pp. 139–181.
- He, J., Chéry, J., 2008. Slip rates of the Altyn Tagh, Kunlun and Karakorum faults (Tibet) from 3D mechanical modeling. *Earth Planet. Sci. Lett.* 274, 50–58.
- Hey, M.H., 1954. A new review of chlorites. *Mineral. Mag.* 30, 277–292.
- Holdsworth, R.E., 2004. Weak faults-rotten cores. *Science* 303, 181–182.
- Holdsworth, R.E., Stewart, M., Imber, J., Strachan, R.A., 2001. The structure and rheological evolution of reactivated continental fault zones: a review and case study. In: Miller, J.A., Holdsworth, R.E., Buick, I.S., Hand, M. (Eds.), *Continental Reactivation and Reworking*. Geological Society, London, pp. 115–137. Special Publications 184, Bath, UK.
- Holdsworth, R.E., van Diggelen, E.W.E., Spiers, C.J., de Bresser, J.H.P., Walker, R.J., Bowen, L., 2011. Fault rocks from the SAFOD core samples: Implications for weakening at shallow depths along the San Andreas Fault, California. *J. Struct. Geology* 33, 132–144.
- Holland, T.J.B., Powell, R., 1998. An internally consistent thermodynamic data set for phases of petrological interest. *J. Metamorph. Geol.* 16, 309–343.

- Houlié, N., Phillips, R.J., 2013. Quaternary rupture behaviour of the Karakoram Fault and its relation to the dynamics of the continental lithosphere, NW Himalaya-Western Tibet. *Tectonophysics* 599, 1–7.
- Ikari, M.J., Marone, C., Saffer, D.M., 2011. On the relation between fault strength and frictional stability. *Geology* 39, 83–86.
- Imber, J., Holdsworth, R.E., Butler, C.A., Lloyd, G.E., 1997. Fault-zone weakening processes along the reactivated Outer Hebrides Fault Zone, Scotland. *J. Geol. Soc. Lond.* 154, 105–109.
- Imber, J., Holdsworth, R.E., Butler, C.A., Strachan, R.A., 2001. A reappraisal of the Sibson-Scholz fault zone model: the nature of the frictional-viscous ('brittle-ductile') transition along a long-lived, crustal-scale fault, Outer Hebrides, Scotland. *Tectonics* 20, 601–624.
- Imber, J., Holdsworth, R.E., Smith, S.A.F., Jefferies, S.P., Collettini, C., 2008. Frictional-viscous flow, seismicity and the geology of weak faults: a review and future directions. In: Wibberley, C.A.J., Kurz, W., Imber, J., Holdsworth, R.E., Collettini, C. (Eds.), *The Internal Structure of Fault Zones: Implications for Mechanical and Fluid-flow Properties*. Geological Society, London, pp. 151–173. Special Publications 299, Bath, UK.
- Jefferies, S.P., Holdsworth, R.E., Wibberley, C.A.J., Shimamoto, T., Spiers, C.J., Niemeijer, A.R., Lloyd, G.E., 2006a. The nature and importance of phyllonite development in crustal-scale fault cores: an example from the Median Tectonic Line, Japan. *J. Struct. Geol.* 28, 220–235.
- Jefferies, S.P., Holdsworth, R.E., Shimamoto, T., Takagi, H., Lloyd, G.E., Spiers, C.J., 2006b. Origin and mechanical significance of foliated cataclastic rocks in the cores of crustal-scale faults: Examples from the Median Tectonic Line, Japan. *J. Geophys. Res.* 11, B12303.
- Jiang, W.T., Peacor, D.R., Buseck, P.R., 1994. Chlorite geothermometry? – contamination and apparent octahedral vacancies. *Clays Clay Minerals* 42, 593–605.
- Klein, E.L., Koppe, J.C., 2000. Chlorite geothermometry and physicochemical conditions of gold mineralization in the Paleoproterozoic Caxias deposit, São Luis craton, northern Brazil. *Geochim. Bras.* 14, 219–232.
- Kranidiotis, P., MacLean, W.H., 1987. Systematics of chlorite alteration at the Phelps Dodge Massive Sulfide Deposit, Matagami, Quebec. *Econ. Geol.* 82, 1898–1911.
- Kronenberg, A.K., Kirby, S.H., Pinkston, J., 1990. Basal slip and mechanical anisotropy of biotite. *J. Geophys. Res. Solid Earth* 95, 19257–19278.
- Kundu, B., Yadav, R.K., Bali, B.S., Chowdhury, S., Gahalaut, V.K., 2014. Oblique convergence and slip partitioning in the NW Himalaya: Implications from GPS measurements. *Tectonics* 33, 2013–2024.
- Lacassin, R., Valli, F., Arnaud, N., Leloup, P.H., Paquette, J.L., Haibing, L., Tapponnier, P., Chevalier, M.-L., Guillot, S., Maheo, G., Zhiqin, X., 2004. Large-scale geometry, offset and kinematic evolution of the Karakoram fault, Tibet. *Earth Planet. Sci. Lett.* 219, 255–269.
- Longstaff, M.A., Meade, B.J., 2014. Edge-driven mechanical microplate models of strike-slip faulting in the Tibetan plateau. *J. Geophys. Res. Solid Earth* 118, 1–11.
- Luan, F.C., Paterson, M.S., 1992. Preparation and deformation of synthetic aggregates of quartz. *J. Geophys. Res.* 97, 301–320.
- Mainprice, D., 1990. An efficient Fortran program to calculate seismic anisotropy from the lattice preferred orientation of minerals. *Comput. Geosci.* 16, 385–393.
- Manatschal, G., 1999. Fluid- and reaction-assisted low-angle normal faulting: evidence from rift-related brittle fault rocks in the Alps (Err Nappe, eastern Switzerland). *J. Struct. Geol.* 21, 777–793.
- Mariani, E., Brodie, K.H., Rutter, E.H., 2006. Experimental deformation of muscovite shear zones at high temperatures under hydrothermal conditions and the strength of phyllosilicate-bearing faults in nature. *J. Struct. Geol.* 28, 1569–1587.
- Marsh, J.H., Johnson, S.E., Yates, M.G., West Jr., D.P., 2009. Coupling of deformation and reactions during mid-crustal shear zone development: an in situ frictional-viscous transition. *J. Metamorph. Geol.* 27, 531–553.
- McCaig, A.M., 1987. Deformation and fluid-rock interaction in metasomatic dilatant shear bands. *Tectonophysics* 135, 121–132.
- Molnar, P., 1988. Continental tectonics in the aftermath of plate tectonics. *Nature* 335, 131–137.
- Moore, D.E., Lockner, D.A., 2004. Crystallographic controls on the frictional behavior of dry and water-saturated sheet structure minerals. *J. Geophys. Res. Solid Earth* 109, B03401.
- Morrow, C.A., Moore, D.E., Lockner, D.A., 2000. The effect of mineral bond strength and adsorbed water on fault gouge frictional strength. *Geophys. Res. Lett.* 27, 815–818.
- Murphy, M.A., Taylor, M.H., Gosse, J., Silver, C.R.P., Whipp, D.M., Beaumont, C., 2014. Limit of strain partitioning in the Himalaya marked by large earthquakes in western Nepal. *Nat. Geosci.* 7, 38–42.
- Neall, F.B., Phillips, G.N., 1987. Fluid-wall interaction in an Archean hydrothermal gold deposit: a thermodynamic model for the Hunt Mine, Kambalda. *Econ. Geol.* 82, 1679–1694.
- Niemeijer, A.R., Spiers, C.J., 2005. Influence of phyllosilicates on fault strength in the brittle-ductile transition: insights from rock analogue experiments. In: Bruhn, D., Burlini, L. (Eds.), *High-strain Zones: Structure and Physical Properties*. Geological Society, London, pp. 303–327. Special Publications 245, Bath, UK.
- Niemeijer, A.R., Spiers, C.J., 2006. Velocity dependence of strength and healing behavior in simulated phyllosilicate-bearing fault gouge. *Tectonophysics* 427, 231–253.
- Niemeijer, A.R., Spiers, C.J., 2007. A microphysical model for strong velocity weakening in phyllosilicate-bearing fault gouges. *J. Geophys. Res. Solid Earth* 112, B10405.
- Niemeijer, A.R., Vissers, R.L.M., 2014. Earthquake rupture propagation inferred from the spatial distribution of fault rock frictional properties. *Earth Planet. Sci. Lett.* 396, 154–164.
- Parry, W.T., Wilson, P.N., Bruhn, R.L., 1988. Pore-fluid chemistry and chemical-reactions on the Wasatch normal-fault, Utah. *Geochim. Cosmochim. Acta* 52, 2053–2063.
- Phartiyal, B., Sharma, A., 2009. Soft-sediment deformation structures in the Late Quaternary sediments of Ladakh: evidence for multiple phases of seismic tremors in the North western Himalayan Region. *J. Asian Earth Sci.* 34, 761–770.
- Phartiyal, B., Sharma, A., Upadhyay, R., Ram-Awatar, Sinha, A.K., 2005. Quaternary geology, tectonics and distribution of palaeo- and present fluvio/glacio lacustrine deposits in Ladakh, NW Indian Himalaya—a study based on field observations. *Geomorphology* 65, 214–256.
- Phillips, R.J., 2008. Geological map of the Karakoram fault zone, Eastern Karakoram, Ladakh, NW Himalaya. *J. Maps* 2008, 38–49.
- Phillips, R.J., Searle, M.P., 2007. Macrostructural and microstructural architecture of the Karakoram fault: relationship between magmatism and strike-slip faulting. *Tectonics* 26, TC3017.
- Phillips, R.J., Parrish, R.R., Searle, M.P., 2004. Age constraints on ductile deformation and long-term slip rates along the Karakoram fault zone, Ladakh. *Earth Planet. Sci. Lett.* 226, 305–319.
- Phillips, R.J., Searle, M.P., Parrish, R.R., 2013. The geochemical and temporal evolution of the continental lithosphere and its relationship to continental-scale faulting: the Karakoram Fault, Eastern Karakoram, NW Himalaya. *Geochim. Geophys. Geosystems* 14, 1525–2027.
- Reichardt, H., Weinberg, R.F., 2012. Hornblende chemistry in Meta- and Diatexites and its Retention in the Source of leucogranites: an example from the Karakoram shear zone, NW India. *J. Petrol.* 53, 1287–1318.
- Rutter, E.H., Hackston, A.J., Yeatman, K.H., Brodie, K.H., Mecklenburgh, J., May, S.E., 2013. Reduction of friction on geological faults by weak-phase smearing. *J. Struct. Geol.* 51, 52–60.
- Rutter, E.H., Holdsworth, R.E., Knipe, R.J., 2001. The nature and tectonics significance of fault-zone weakening: an introduction. In: Holdsworth, R.E., Strachan, R.A., Magloughlin, J.F., Knipe, R.J. (Eds.), *The Nature and Tectonic Significance of Fault Zone Weakening*. Geological Society, London, pp. 1–11. Special Publications 186, Bath, UK.
- Schiffman, P., Fridleifsson, G.O., 1991. The smectite-chlorite transition in drillhole NJ-15, Nesjavellir geothermal field, Iceland: XRD, BSE and electron microprobe investigations. *J. Metamorph. Geol.* 9, 679–696.
- Scholz, C.H., 1988. The brittle-plastic transition and the depth of seismic faulting. *Geol. Rundsch.* 77, 319–328.
- Scholz, C.H., 2002. *The Mechanics of Earthquakes and Faulting*, Second ed. Cambridge University Press, Cambridge, UK.
- Schrank, C.E., Handy, M.R., Fosseis, F., 2008. Multiscale of shear zones and the evolution of the brittle-to-viscous transition in continental crust. *J. Geophys. Res. Solid Earth* 113, B01407.
- Searle, M.P., Elliott, J.R., Phillips, R.J., Chung, S.-L., 2011. Crustal-lithospheric structure and continental extrusion of Tibet. *J. Geol. Soc. Lond.* 168, 633–672.
- Searle, M.P., Weinberg, R.F., Dunlap, W.J., 1998. Transpressional tectonics along the Karakoram fault zone, northern Ladakh: constraints on Tibetan extrusion. In: Holdsworth, R.E., Strachan, R.A., Dewey, J.F. (Eds.), *Continental Transpressional and Transtensional Tectonics*. Geological Society, London, pp. 307–326. Special Publications 135, Bath, UK.
- Searle, M.P., Parrish, R.R., Thow, A.V., Noble, S.R., Phillips, R.J., Waters, D.J., 2010. Anatomy, age and evolution of a collisional mountain belt: the Baltoro granite batholith and Karakoram Metamorphic Complex, Pakistani Karakoram. *J. Geol. Soc. Lond.* 167, 183–202.
- Sen, K., Mukherjee, B.K., Collins, A.S., 2014. Interplay of deformation and magmatism in the Pangong Transpressional Zone, eastern Ladakh, India: Implications for remobilization of the trans-Himalayan magmatic arc and initiation of the Karakoram Fault. *J. Struct. Geol.* 62, 13–24.
- Shigematsu, N., Fujimoto, K., Tanaka, N., Furuya, N., Mori, H., Wallis, S., 2012. Internal structure of the Median Tectonic Line fault zone, SW Japan, revealed by borehole analysis. *Tectonophysics* 532, 103–118.
- Sibson, R.H., 1986. Earthquakes and rock deformation in crustal fault zones. *Annu. Rev. Earth Planet. Sci.* 14, 149–175.
- Stewart, M., Strachan, R.A., Holdsworth, R.E., 1999. The structure and early kinematic history of the Great Glen Fault Zone, Scotland. *Tectonics* 18, 326–342.
- Stewart, M., Holdsworth, R.E., Strachan, R.A., 2000. Deformation processes and weakening mechanisms within the frictional-viscous transition zone of major crustal-scale faults: insights from the Great Glen Fault Zone, Scotland. *J. Struct. Geol.* 22, 543–560.
- Streule, M.J., Phillips, R.J., Searle, M.P., Waters, D.J., Horstwood, M.S.A., 2009. Evolution and chronology of the Pangong Metamorphic Complex adjacent to the Karakoram Fault, Ladakh: constraints from thermobarometry, metamorphic modelling and U Pb geochronology. *J. Geol. Soc.* 166, 919–932.
- Tapponnier, P., Molnar, P.J., 1976. Slip-line field theory and large-scale continental tectonics. *Nature* 264, 319–324.
- Thakur, V.C., 1981. Regional framework and geodynamic evolution of the Indus-Tsangpo suture zone in the Ladakh Himalayas. *Trans. R. Soc. Edinb. Earth Sci.* 72, 89–97.
- Thatcher, W., 2009. How the Continents deform: the evidence from tectonic geodesy. *Annu. Rev. Earth Planet. Sci.* 37, 237–262.

- Upadhyay, R., 2001. Seismically-induced soft-sediment deformational structures around Khalsar in the Shyok Valley, northern Ladakh and eastern Karakoram, India. *Curr. Sci.* 81, 600–604.
- Upadhyay, R., 2003. Earthquake-induced soft-sediment deformation in the lower Shyok river valley, northern Ladakh, India. *J. Asian Earth Sci.* 21, 413–421.
- Valli, F., Leloup, P.H., Paquette, J.-L., Arnaud, N., Li, H., Tapponnier, P., Lacassin, R., Guillot, S., Liu, D., Deloule, E., Xu, Z., Mahéo, G., 2008. New U-Th/Pb constraints on timing of shearing and long-term slip-rate on the Karakorum fault. *Tectonics* 27, TC5007.
- Van Diggelen, E.W.E., De Bresser, J.H.P., Peach, C.J., Spiers, C.J., 2010. High shear strain behaviour of synthetic muscovite fault gouges under hydrothermal conditions. *J. Struct. Geol.* 32, 1685–1700.
- Wallis, D., Phillips, R.J., Lloyd, G.E., 2013. Fault weakening across the frictional-viscous transition zone, Karakoram Fault Zone, NW Himalaya. *Tectonics* 32, 1227–1246.
- Wallis, D., Parsons, A.J., Phillips, R.J., Searle, M.P., Ferré, E., 2014a. Comment on “Interplay of deformation and magmatism in the Pangong Transpressional Zone, Eastern Ladakh, India: Implications for remobilization of the trans-Himalayan magmatic arc and initiation of the Karakoram Fault” by K. Sen, B.K. Mukherjee and A.S. Collins. *J. Struct. Geol.* 62, 13–24. *Journal of Structural Geology* 65, 117–119.
- Wallis, D., Phillips, R.J., Lloyd, G.E., 2014b. Evolution of the Eastern Karakoram Metamorphic Complex, Ladakh, NW India, and its relationship to magmatism and regional tectonics. *Tectonophysics* 626, 41–52.
- Wang, S., Wang, E., Fang, X., Lai, Q., 2011. U-Pb SHRIMP and  $^{40}\text{Ar}/^{39}\text{Ar}$  ages constrain the deformation history of the Karakoram fault zone (KFZ), SW Tibet. *Tectonophysics* 509, 208–217.
- Whipp Jr., D.M., Beaumont, C., Braun, J., 2014. Feeding the “aneurysm”: orogen-parallel mass transport into Nanga Parbat and the western Himalayan syntaxis. *J. Geophys. Res. Solid Earth* 119, 5077–5096.
- White, S.R., 2001. Textural and microstructural evidence for semi-brittle flow in natural fault rocks with varied mica contents. *Int. J. Earth Sci.* 90, 14–27.
- White, S.R., Knipe, R.J., 1978. Transformation- and reaction-enhanced ductility in rocks. *J. Geol. Soc.* 135, 513–516.
- Wibberley, C.A.J., 2005. Initiation of basement thrust detachments by fault-zone reaction weakening. In: Bruhn, D., Burlini, L. (Eds.), *High Strain Zones: Structure and Physical Properties*. Geological Society, London, pp. 347–372. Special Publications 245, Bath, UK.
- Wintsch, R.P., Christoffersen, R., Kronenberg, A.K., 1995. Fluid-rock reaction weakening of fault zones. *J. Geophys. Res.* 100, 13021–13032.
- Wintsch, R.P., Yeh, M.W., 2013. Oscillating brittle and viscous behavior through the earthquake cycle in the Red River Shear Zone: monitoring flips between reaction and textural softening and hardening. *Tectonophysics* 587, 46–62.
- Zhang, R., Murphy, M.A., Lapen, T.J., Sanchez, V., Heizler, M., 2011. Late Eocene crustal thickening followed by Early-Late Oligocene extension along the India-Asia suture zone: evidence for cyclicity in the Himalayan orogen. *Geosphere* 7, 1249–1268.
- Zang, W., Fyfe, W.S., 1995. Chloritization of the hydrothermally altered bedrock at the Igarapé Bahia gold deposit, Carajás, Brazil. *Miner. Deposita* 30, 30–38.